Functionally-Coupled Ion Channels Begin Co-assembling at the Start of Their Synthesis

Authors:

Roya Pournejati[1,2], Jessica M. Huang[1,2], Michael Ma[1,2], Claudia M. Moreno[2,3], Oscar Vivas[1,2*]

Affiliations:

[1] Department of Pharmacology, University of Washington

[2] Department of Neurobiology and Biophysics, University of Washington

[3] Howard Hughes Medical Institute

***Corresponding author:**

Oscar Vivas

Department of Pharmacology

Department of Neurobiology and Biophysics

University of Washington, School of Medicine

Box 357290

Seattle, WA 98195-7290

Email: vivas@uw.edu

Phone: (206) 543-0958

Summary

Calcium binding to BK channels lowers BK activation threshold, substantiating functional coupling with calcium-permeable channels. This coupling requires close proximity between different channel types, and the formation of BK–$Ca_V1.3$ hetero-clusters at nanometer distances exemplifies this unique organization. To investigate the structural basis of this interaction, we tested the hypothesis that BK and $Ca_V1.3$ channels assemble before their insertion into the plasma membrane. Our approach incorporated four strategies: (1) detecting interactions between BK and $Ca_V1.3$ proteins inside the cell, (2) identifying membrane compartments where intracellular hetero-clusters reside, (3) measuring the proximity of their mRNAs, and (4) assessing protein interactions at the plasma membrane during early translation. These analyses revealed that a subset of BK and $Ca_V1.3$ transcripts are spatially close in micro-translational complexes, and their newly synthesized proteins associate within the endoplasmic reticulum (ER) and Golgi. Comparisons with other proteins, transcripts, and randomized localization models support the conclusion that BK and $Ca_V1.3$ hetero-clusters form before their insertion at the plasma membrane.

Significance statement

This work examines the proximity between BK and $Ca_V1.3$ molecules at the level of their mRNAs and newly synthesized proteins to reveal that these channels interact early in their biogenesis. Two cell models were used: a heterologous expression system to investigate the steps of protein trafficking and a pancreatic beta cell line to study the localization of endogenous channel mRNAs. Our findings show that BK and $Ca_V1.3$ channels begin assembling intracellularly before reaching the plasma membrane, revealing new aspects of their spatial organization. This intracellular assembly suggests a coordinated process that contributes to functional coupling.

Introduction

This work concerns the organization of functionally coupled voltage- and calcium-dependent potassium (BK) channels and voltage-gated calcium (Ca_V) channels.

BK channels (a.k.a. $K_{Ca}1.1$, Maxi-K, Slo1, KCNMA1) are named for their "big potassium (K^+)" conductance, since channel opening leads to unusually large, outward potassium currents and membrane repolarization. Its amino acid sequence is conserved throughout the animal kingdom from worms to mammals. BK channels are expressed in a wide variety of cell types, predominantly excitable cells but also non-excitable salivary, bone and kidney cells, making this channel responsible for a large range of physiological processes [1-9]. Phenotypes of pathological BK mutations in human patients are most prominent in the brain and muscle and often manifest as seizures, movement disorders, developmental delay, and intellectual disability [10, 11]. BK is also implicated in other organ system functions, including but not limited to heart pace making, reproduction, and pancreatic glucose homeostasis [11, 12].

Since BK channels affect function in numerous physiological systems, channel opening is meticulously regulated at the cellular level. BK is a voltage-gated channel activated by membrane depolarization. Interestingly, BK has an additional gating mechanism that differentiates it from typical voltage-gated potassium channels; BK opening is gated by both voltage and intracellular calcium binding to a cytosolic regulatory domain. At the cytoplasmic resting free calcium concentration (~0.1 μM), BK channels remain closed [13]. However, the probability of channel opening increases when both the membrane potential depolarizes and when the local free calcium rises. Yet, increases of calcium are tightly limited by endogenous proteins that bind calcium with high affinity as well as by extrusion mechanisms that take calcium inside organelles or outside the cell. Hence, the activation of BK channels relies on strategies to overcome these regulatory barriers. One such strategy is to localize near sources of calcium.

In excitable cells, BK forms nanodomains with calcium channels that provide exclusive, localized calcium sources. Several subtypes of calcium channels form functional signaling complexes with BK, shifting BK activation voltages to more negative potentials [14-16]. One of these channels, $Ca_V1.3$ (a.k.a. *CACNA1D*), is unique in its electrophysiological profile as an L-type calcium channel, activating with fast kinetics at voltages as negative as -55 mV [17]. Additionally, BK channels are modulated by auxiliary subunits, which fine-tune BK channel gating properties to adapt to different physiological conditions. The β, γ, and LINGO1 subunits each contribute distinct structural and regulatory features: β-subunits modulate Ca^{2+} sensitivity and can induce inactivation; γ-subunits shift voltage-dependent activation to more negative potentials; and LINGO1 reduces surface expression and promotes rapid inactivation. These interactions ensure

87 precise control over channel activity, allowing BK channels to integrate voltage and calcium
88 signals dynamically in various cell types [18-24].
89 Here, we focus on the selective assembly of BK channels with $Ca_V1.3$ and do not evaluate
90 the contributions of auxiliary subunits to BK channel organization. $Ca_V1.3$ is expressed in many
91 of the same cell types as BK and is often functionally coupled with BK channels, enabling BK
92 channels to activate at more negative voltages. Notably, super-resolution microscopy shows that
93 $Ca_V1.3$ organizes spatially into nanodomains with BK in the plasma membrane [15]. However, the
94 mechanisms behind the assembly of BK and $Ca_V1.3$ hetero-clusters are unknown.

Mechanism	**Description**	**Source**
Co-translation of heteromeric channel subunits	mRNA transcripts and nascent proteins of hERG heteromeric subunits form molecular complexes during protein translation.	[25]
Co-translation of channels permeating different ions	Potassium channel hERG and sodium channel SCN5A form complexes of mRNA transcripts and nascent proteins during protein translation.	[26]
Membrane curvature sensing	Clusters of Piezo1 channels enriche in membrane invaginations.	[27]
ER membrane protein complex	ER membrane complex acts as a chaperone for heteromeric channel assembly	[28]
Scaffolding proteins	Scaffolding protein AKAP150 is required for abnormal gating of $Ca_V1.2$-LQT8 channels.	[29]
Random insertion	Clusters of $Ca_V1.2$, $Ca_V1.3$, BK, and TRPV4 are proposed to be randomly formed into the plasma membranes of smooth muscle, cardiac muscle, hippocampal neurons, and tsA-201 cells.	[30]

95
96 **Table 1.** List of mechanisms described for the interaction between channel subunits, channels of the
97 same type (homo-clusters), or hetero-clusters of channel families permeating different ions.
98
99 Several mechanisms for bringing ion channels together have been suggested (Table 1).
100 One proposes that proteins assembly precedes protein insertion into the plasma membrane [25,
101 26, 31]. This mechanism has been observed in studies of hetero-multimers and even channels
102 permeating different ions. The formation of these groups of proteins would start from their
103 synthesis. There is even the possibility of mRNA transcripts colocalizing prior to translation. We

104 explored this mechanism in relation to BK and $Ca_V1.3$ functional coupling. Here, we started by
105 investigating when and where BK and $Ca_V1.3$ channels cluster in the cell. We looked for BK and
106 $Ca_V1.3$ hetero-clusters at intracellular membranes of the ER, at ER exit sites, and at the Golgi.
107 We also investigated the proximity between mRNA transcripts of BK and $Ca_V1.3$.

108 **Definitions used in this manuscript**

109 To guide the reader and prevent confusion on the terms used, we introduce the following
110 nomenclature, which is also illustrated in Figure 1. Molecular complex: an array of several
111 polypeptides with a defined function. In our case, a BK channel is a molecular complex of four
112 alpha subunits whose function is to permeate ions. Homo-cluster: we define a homo-cluster as
113 the accumulation of proteins. In our work, a homo-cluster refers to the accumulation of BK
114 channels or the accumulation of calcium channels.

115 Hetero-cluster: we define a hetero-cluster as the collection of different types of proteins
116 that facilitate functional coupling and compartmentalization of a signaling complex. In the present
117 work, hetero-cluster refers to a coordinated collection of BK and Ca_V channels. It is also used to
118 refer to the assembly of homo-clusters of BK with homo-clusters of Ca_V channels.

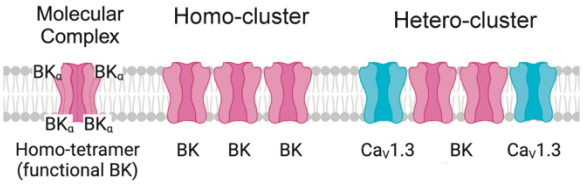

Figure 1. Representation of molecular complex, homo-cluster, and hetero-cluster.

119

120 **Results**

121 **BK and $Ca_V1.3$ hetero-clusters are found inside the cell.**

122 BK and Ca_V hetero-clusters have been observed at the plasma membrane [14-16].
123 However, a clear understanding of when or how BK and Ca_V hetero-clusters assemble is missing.
124 A simple mechanism proposes that these hetero-clusters organize only at the plasma membrane.
125 Here, we tested the alternative hypothesis of BK and Ca_V assembling inside the cell (Figure 2A).
126 To test this idea, we used proximity ligation assay (PLA) and antibodies against BK and $Ca_V1.3$
127 channels. When these antibodies are within 40 nm of each other, PLA ligation and amplification
128 can occur, resulting in the formation of fluorescent puncta (Figure 2B), here referred to as PLA
129 puncta. Hence, the PLA puncta in Figure 2C represent BK and $Ca_V1.3$ hetero-clusters. To confirm
130 specificity, a negative control was performed by probing only for BK using the primary antibody,
131 ensuring that detected signals were not due to non-specific binding or background fluorescence.
132 We first analyzed Z-projections, in which all the puncta in the cell volume are added, and found a

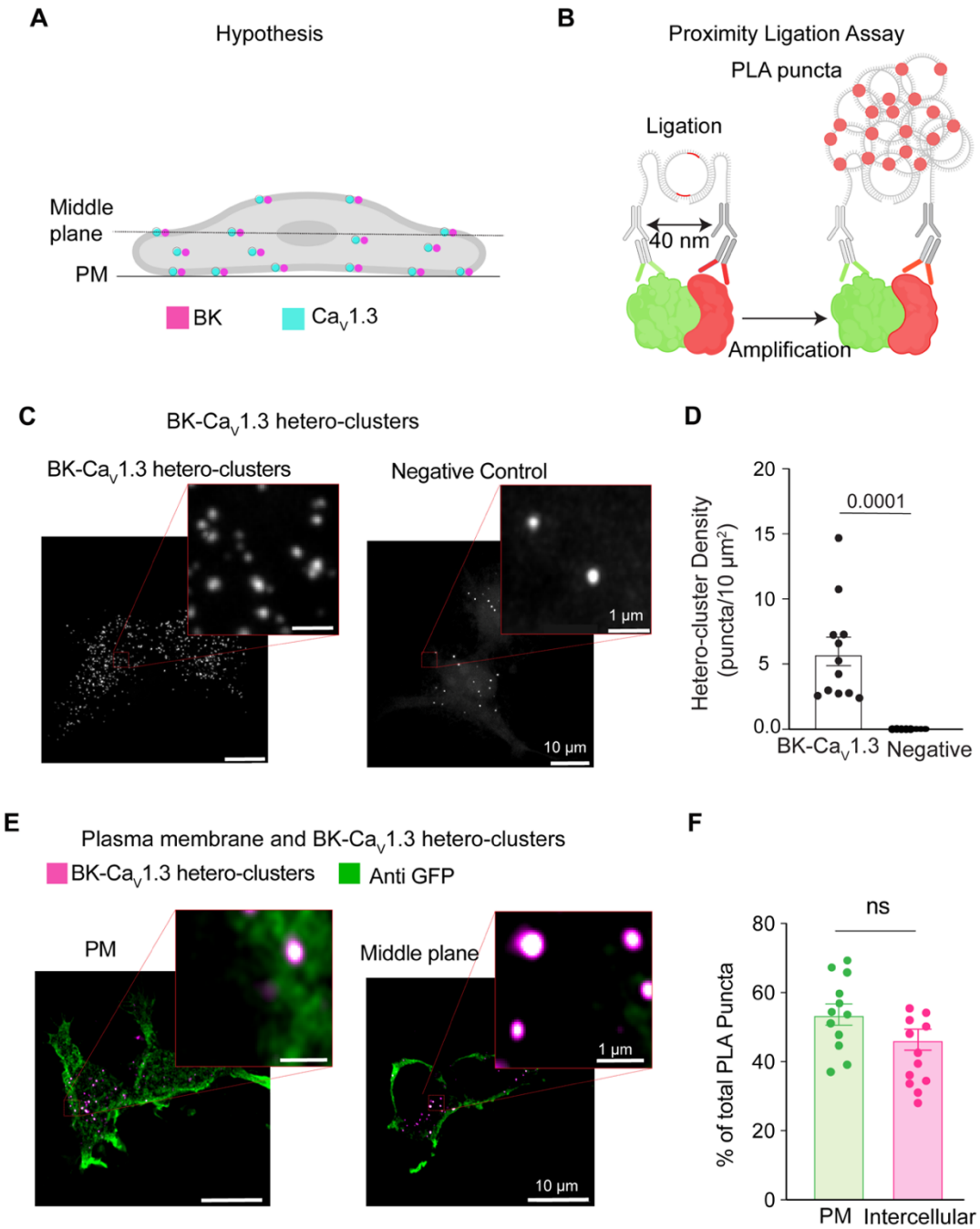

Figure 2. BK and Ca$_V$1.3 hetero-clusters are found inside the cell. A. Diagram of the hypothesis: hetero-clusters of BK (magenta) and Ca$_V$1.3 (cyan) are on intracellular membranes and on the plasma membrane. **B.** Illustration of the technique to detect BK and Ca$_V$1.3 hetero-clusters. Proximity ligation assay is used to detect the hetero-clusters. **C.** Confocal images of fluorescent puncta from PLA experiments in tsA-201 cells. Left: Cells were transfected and probed for BK and Ca$_V$1.3 channels. Right: negative control. Cells were transfected and probed only for BK channels. Enlargement of a selected region is shown in the inset. **D.** Scatter dot plot comparing puncta density of BK and Ca$_V$1.3 hetero-clusters to the negative control. Data points are from n = 12 cells for BK and Ca$_V$1.3 hetero-clusters and from n = 14 cells for negative control. *p*-values are shown at the top of the graphs. **E.** Confocal images of fluorescent PLA puncta at different focal planes co-labeled against GFP at the plasma membrane. Cells were transfected with BK, Ca$_V$1.3, and PH-PLCδ-GFP and probed for BK channels, Ca$_V$1.3 channels, and GFP. PLA puncta are shown in magenta, and the plasma membrane is shown in green. Enlargements of the representative regions of PM and intercellular hetero-clusters are shown in the insets. **F.** Scatter dot plot comparing BK and Ca$_V$1.3 hetero-cluster abundance at PM and inside the cell. Data points are from n = 12 cells. Scale bar is 10 µm and 1 µm in the insets. For statistical analysis, unpaired t-tests were applied in panel D and paired t-tests in panel F to evaluate significance.

density of 5.8 ± 1.0 / 10 μm^2. In a different experiment, we analyzed the puncta density for each focal plane of the cell (step size of 300 nm) and compared the puncta at the plasma membrane to the rest of the cell. We visualized the plasma membrane with a biological sensor tagged with GFP (PH-PLCδ-GFP) and then probed it with an antibody against GFP (Figure 2E). By analyzing the GFP signal, we created a mask that represented the plasma membrane. The mask served to distinguish between the PLA puncta located inside the cell and those at the plasma membrane, allowing us to calculate the number of PLA puncta at the plasma membrane. To our surprise, we found a significant number of puncta localized inside the cell. 46 ± 3 % of the puncta were localized intracellularly, whereas 54 ± 3 % were at the plasma membrane. This finding is consistent with our supposition that BK and $Ca_V1.3$ channels colocalize in the cell.

BK and $Ca_V1.3$ hetero-clusters localize at ER and ER exit sites.

We next investigated the identity of the intracellular membranes where these PLA puncta were found. A large component of intracellular membranes in the cell is the endoplasmic reticulum (ER), where channels are inserted after translation. To determine whether BK and $Ca_V1.3$ associate in the ER (Figure 3A), we combined PLA with immunodetection. As before, PLA probed for BK and $Ca_V1.3$ hetero-clusters, while a KDEL-moxGFP label identified the ER (Figure 3B). To avoid disruption of organelle architecture, we used the monomeric mox version of KDEL-GFP, which is optimized to reduce oligomerization in the ER environment [33]. Neither overexpression of KDEL-moxGFP nor fixation altered the ER structure as the tubule width remained around 150 nm for either condition (Figure 3C), a value in agreement with the literature [34, 35]. To assess the percentage of PLA puncta colocalizing with the ER, we employed two different cell lines, our overexpression system (tsA-201 cells) and a rat insulinoma cell line (INS-1) that expresses BK and $Ca_V1.3$ channels endogenously. In this and following experiments, we analyze one focal plane, in the middle of the cell, to quantify PLA puncta colocalization with ER membrane. Figure 3D shows PLA puncta in the same space as the ER. Comparing the overexpression and endogenous systems, 63 ± 3% versus 50 ± 6% of total PLA puncta were localized at the ER (Figure 3E). To determine whether the observed colocalization between BK–$Ca_V1.3$ hetero-clusters and the ER was not simply due to the extensive spatial coverage of ER labeling, we labeled ER exit sites using Sec16-GFP and probed for hetero-clusters with PLA. This approach enabled us to test whether the hetero-clusters were preferentially localized to ER exit sites, which are specialized trafficking hubs that mediate cargo selection and direct proteins from the ER into the secretory pathway. In contrast to the more expansive ER network, which supports protein synthesis and folding, ER exit sites ensure efficient and selective export of proteins to their target

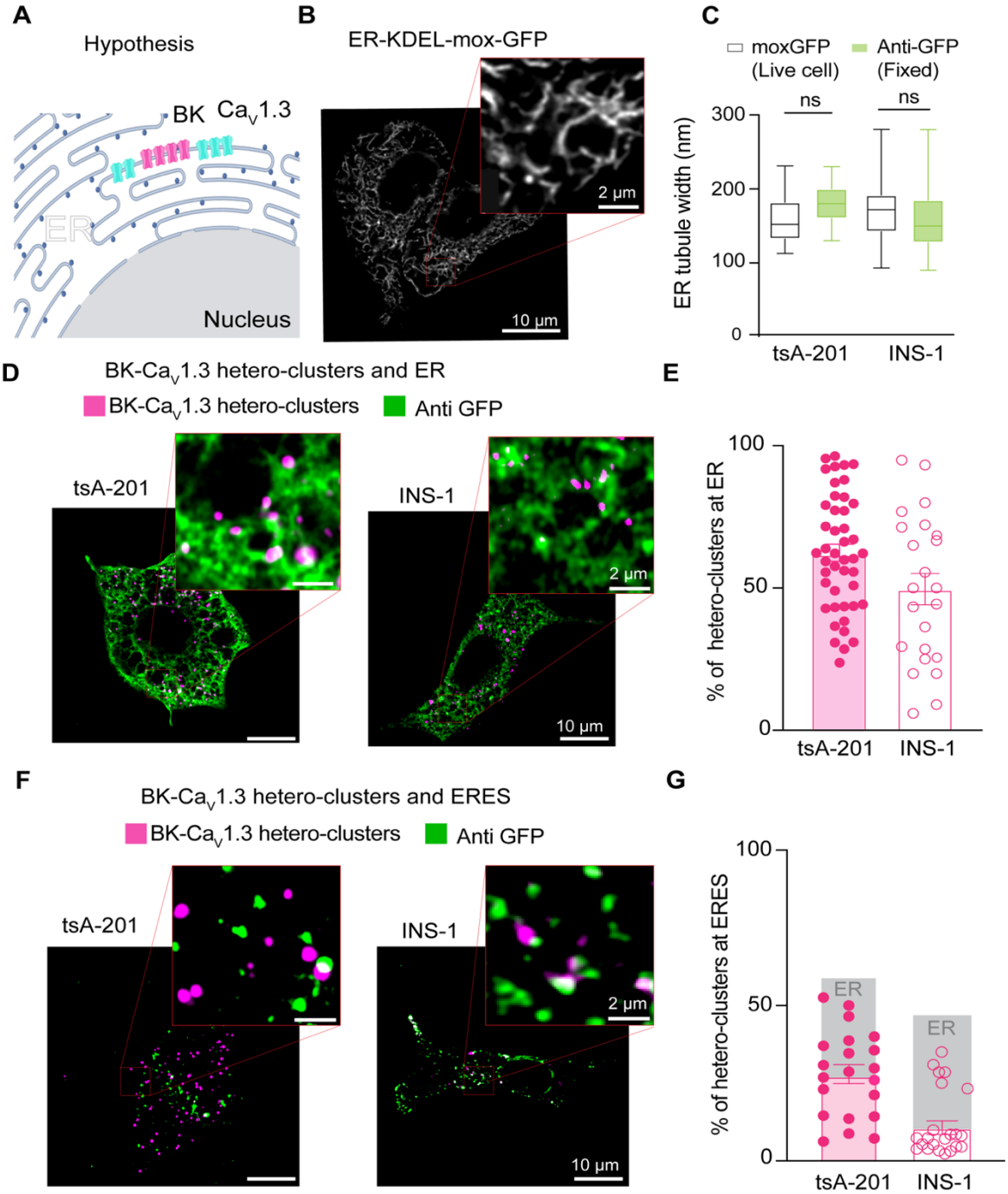

Figure 3. BK and $Ca_V1.3$ hetero-clusters localize at ER and ER exit sites (ERES). A. Diagram of the hypothesis: hetero-clusters of BK (magenta) and $Ca_V1.3$ (cyan) can be found at the ER membrane. **B.** Representative image of the ER labeled with exogenous GFP in INS-1 cells. Cells were transfected with KDEL-moxGFP. Magnification is shown in the inset. **C.** Comparison of the ER tubule distance in live and fixed tsA-201 and INS-1 cells. Data points are from n = 23 tsA-201 cells, n = 27 INS-1 cells **D.** Representative images of PLA puncta and ER. Left: tsA-201 cells were transfected with BK, $Ca_V1.3$ and KDEL-moxGFP. Right: INS-1 cells were transfected only with KDEL-moxGFP. Fixed cells were probed for BK-$Ca_V1.3$ hetero-clusters (PLA puncta) and GFP. PLA puncta is shown in magenta. ER is shown in green. **E.** Comparison of BK-$Ca_V1.3$ hetero-clusters found at the ER and relative to all PLA puncta in the cell. Values are given in percentages. **F.** Representative images of PLA puncta and ER exit sites. Left and right are the same as in D, but cells were transfected with Sec16-GFP instead of KDEL. **G.** Comparison of BK-$Ca_V1.3$ hetero-clusters found at ER exit sites relative to all PLA puncta in the cell. Values are given in percentages. Data points are from n = 45 tsA-201 cells for ER, n = 21 tsA-201 cells for ERES, n = 23 INS-1 cells for ER, and n = 23 INS-1 cells for ER exit sites. Scale bar is 10 µm and 2 µm in the magnifications.

168

169 destinations. By quantifying the proportion of BK and $Ca_V1.3$ hetero-clusters relative to
170 total channel expression at ER exit sites, we found 28 ± 3% colocalization in tsA-201 cells and 11
171 ± 2% in INS-1 cells (Figure 3F). While the percentage of colocalization between hetero-clusters
172 and the ER or ER exit sites alone cannot be directly compared to infer trafficking dynamics, these
173 findings reinforce the conclusion that hetero-clusters reside within the ER and suggest that BK
174 and $Ca_V1.3$ channels traffic together through the ER and exit in coordination.
175
176 **BK and $Ca_V1.3$ hetero-clusters go through the Golgi.**
177 Channels are modified in the Golgi after synthesis (Figure 4A), so we asked whether PLA
178 puncta formed by BK and $Ca_V1.3$ hetero-clusters can be found in the Golgi. Using the same
179 strategy, we labeled Golgi with Gal-T-mEGFP (Figure 4B) and detected BK-$Ca_V1.3$ hetero-
180 clusters using PLA. To confirm that the overexpressed Gal-T-mEGFP labels the Golgi specifically
181 without altering its structure, we compared the region detected by the antibody against GFP to
182 the region detected by a primary antibody against the Golgi protein 58K (Figure 4C). 58K is a
183 specific peripheral protein that localizes to the cytosolic face of Golgi [36]. The overlay shows that
184 the GFP signal labels the same region as the antibody against 58K. When assessing the presence
185 of BK-$Ca_V1.3$ hetero-clusters in the Golgi, we found that 31 ± 5% of PLA puncta were localized at
186 the Golgi in the overexpression system and 25 ± 4% in the endogenous cell model (Figure 4E).
187 We performed controls to confirm that the formation of hetero-clusters between the two
188 channels was not coincidental but rather the result of structural coupling. We tested the formation
189 of PLA puncta between BK channels and the Golgi protein 58K. We also tested for $Ca_V1.3$ and
190 58K. We did not find PLA puncta when the proximity between the channels and 58K was probed
191 (Figure 4F), supporting the idea that PLA puncta between BK and $Ca_V1.3$ channels found at the
192 Golgi represent specific coupling. We selected the Golgi as a control because it represents the
193 final stage of protein trafficking, ensuring that hetero-cluster interactions observed at this point
194 reflect specificity maintained throughout earlier trafficking steps, including within the ER. As an
195 additional control, we tested the formation of PLA puncta between $Ca_V1.3$ channels and RyR_2, a
196 protein localized in the ER. The number of PLA puncta between $Ca_V1.3$ and RyR_2 was significantly
197 lower than the number observed between $Ca_V1.3$ and BK channels (Figure 4-Supplement 1),
198 further supporting the specificity of BK–$Ca_V1.3$ interactions.
199 It is important to clarify that the percentages provided in this work cannot be added up to
200 understand the distribution of hetero-clusters along the biosynthetic pathway of the channels. The
201 percentage in each membrane compartment was compared to the total percentage of hetero-
202 clusters observed in each cell for that particular experiment. Therefore, there is expected overlap

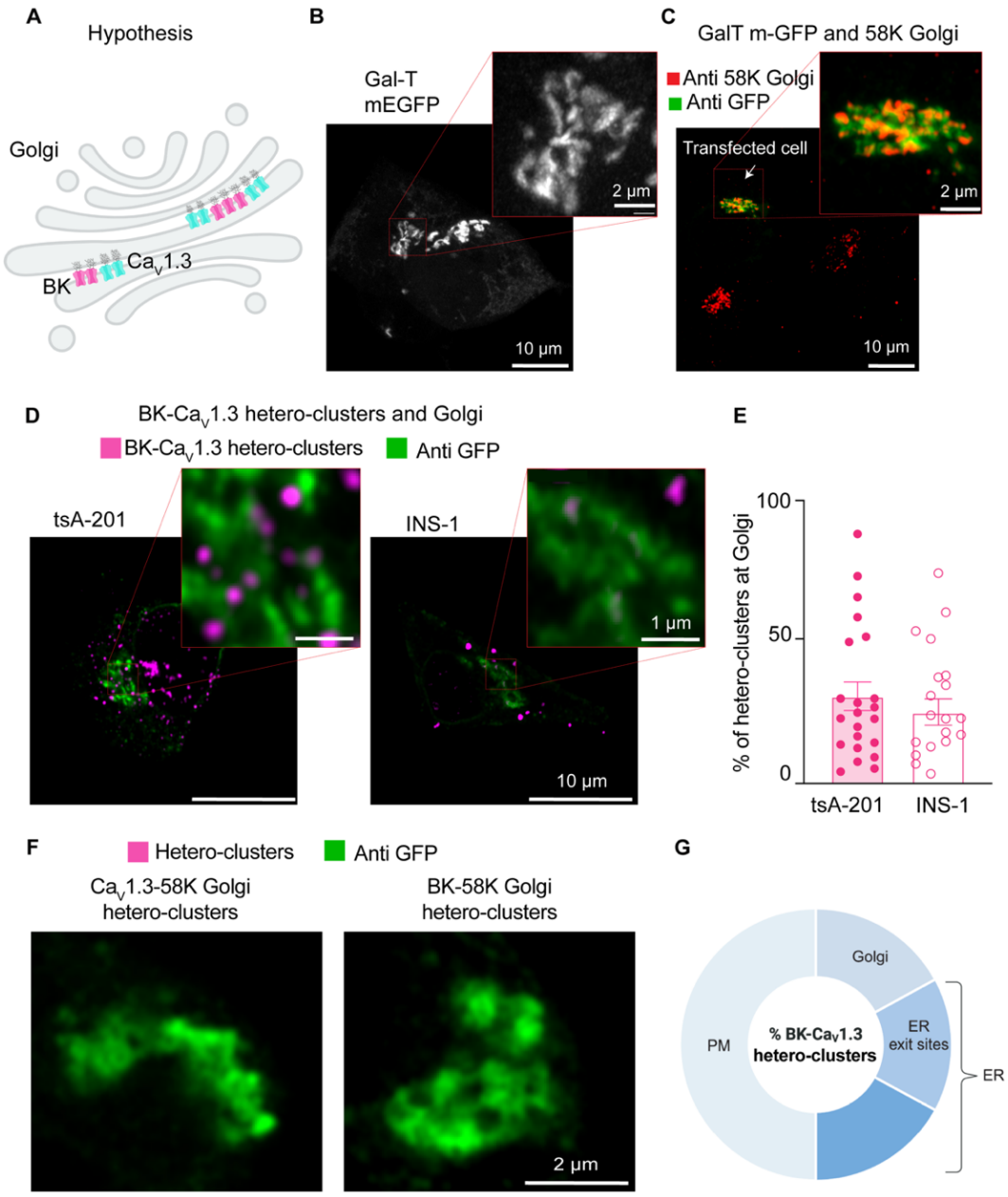

Figure 4. BK and Ca$_V$1.3 hetero-clusters go through the Golgi. A. Diagram of the hypothesis: PLA puncta detecting hetero-clusters between BK (magenta) and Ca$_V$1.3 (cyan) channels can be found at the Golgi membrane. **B.** Representative image of the Golgi structure with exogenous GFP in INS-1 cells. Cells were transfected with Gal-T-mEGFP. Enlargement is shown in the inset. **C.** Representative images of fixed cells co-stained with antibodies against Gal-T-mEGFP in green and 58K-Golgi in red **D.** Representative images of PLA puncta and Golgi. tsA-201 cells were transfected with BK, Ca$_V$1.3 and Gal-T-mEGFP (left), and INS-1 cells were transfected only with Gal-T-mEGFP (right). PLA puncta are shown in magenta. Golgi is shown in green. **E.** Scatter dot plot of percentages of BK-Ca$_V$1.3 hetero-clusters found at the Golgi relative to all PLA puncta in tsA-201 and INS1 cells. Data points are from n = 22 tsA-201 cells and n = 19 INS-1 cells. **F.** Representative image of PLA puncta and Golgi. tsA-201 cells were transfected with BK, Ca$_V$1.3, and Gal-T-mEGFP. Left: PLA was done against BK and 58K Golgi (magenta), and Golgi is shown in green. Right: PLA was done against Ca$_V$1.3 and 58K Golgi (magenta), and Golgi is shown in green. **G.** Diagram illustrating our interpretation of percentages of BK-Ca$_V$1.3 hetero-clusters found in the cell. This illustration is based on results shown in Figures 1-4. Percentages were modified to represent overlap of fluorescent signals and limited resolution. We also show that hetero-clusters found in the ER exit sites (ERES) are also accounted in the ER. Scale bars: 10 µm and 2 µm in panels B and C; 10 µm and 1 µm in panel D; 2 µm in panel F.

203

204 between our measurements due to (1) optical resolution and (2) the effect of not comparing all
205 the organelles in the same cell. Considering these limitations, we interpreted our results as
206 follows: about one half of hetero-clusters are found inside the cell. The other half corresponds to
207 hetero-clusters at the plasma membrane. From the half inside the cell, roughly one third of hetero-
208 clusters is found in the Golgi, and another third is found in ER exit sites (Figure 4G). The remaining
209 hetero-clusters are found in other regions of the ER and in membranes that we did not probe,
210 such as vesicles. Finally, a key limitation of this approach is that we cannot quantify the proportion
211 of total BK or $Ca_V1.3$ channels engaged in hetero-clusters within each compartment. The PLA
212 method provides proximity-based detection, which reflects relative localization rather than
213 absolute channel abundance within individual organelles.

214 **BK mRNA and $Ca_V1.3$ mRNA colocalize.**

215 How is it that BK and $Ca_V1.3$ proteins come in close proximity in membranes of the ER,
216 ER exit sites and the Golgi? To explore the origins of the initial association, we hypothesized that
217 the two proteins are translated near each other, which could be detected as the colocalization of
218 their mRNAs (Figure 5A and B). The experiment was designed to detect single mRNA molecules
219 from INS-1 cells in culture. We performed multiplex in situ hybridization experiments using an
220 RNAscope fluorescence detection kit to be able to image three mRNAs simultaneously in the
221 same cell and acquired the images in a confocal microscope with high resolution. To rigorously
222 assess the specificity of this potential mRNA-level organization, we used multiple internal controls.
223 *GAPDH* mRNA, a highly expressed housekeeping gene with no known spatial coordination with
224 channel mRNAs, served as a baseline control for nonspecific colocalization due to transcript
225 abundance. To evaluate whether the spatial proximity between BK mRNA (*KCNMA1*) and $Ca_V1.3$
226 mRNA (*CACNA1D*) was unique to functionally coupled channels, we also tested for $Na_V1.7$ mRNA
227 (*SCN9A)*, a transmembrane sodium channel expressed in INS-1 cells but not functionally
228 associated with BK. This allowed us to determine whether the observed colocalization reflected
229 a specific biological relationship rather than shared expression context. Finally, to test whether
230 this proximity might extend to other calcium sources relevant to BK activation, we probed the
231 mRNA of ryanodine receptor 2 (*RyR2*), another Ca^{2+} channel known to interact structurally with
232 BK channels [37]. Together, these controls were chosen to distinguish specific mRNA
233 colocalization patterns from random spatial proximity, shared subcellular distribution, or gene
234 expression level artifacts. Figure 5- Supplementary-2 shows images completely void of
235 fluorescent signal from INS-1 cells probed for bacterial mRNA (negative control, Figure 5-
236 Supplementary 2A) and shows images of INS-1 cells probed for mammalian mRNAs expected to
237 be in these cells (positive control, Figure 5- Supplementary 2B). We confirmed the specificity of

238 the probes by performing in situ hybridization against *KCNMA1*, *CACNA1D*, *RyR2*, and *SCN9A*
239 in non-transfected cell lines (Figure 5- Supplementary 2C and D).

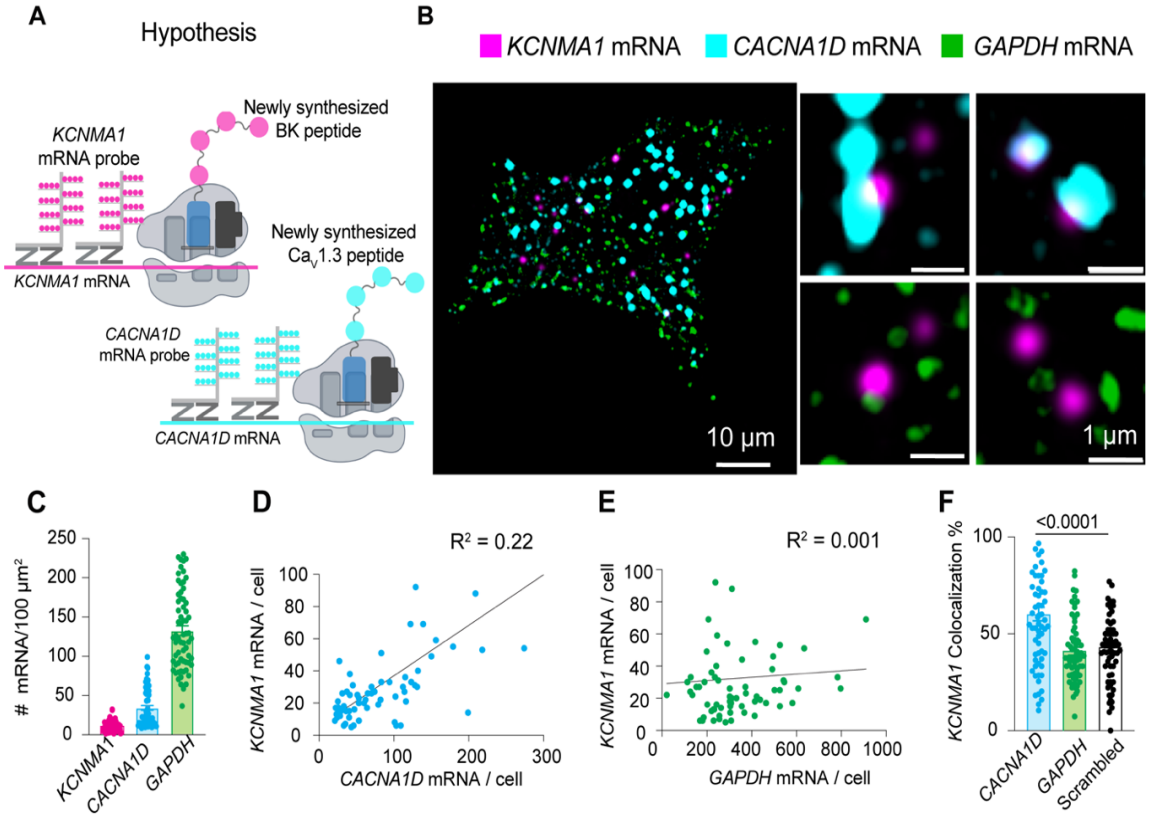

Figure 5. BK mRNA (*KCNMA1*) and Ca$_V$1.3 mRNA (*CACNA1D*) colocalize. A. Diagram of the hypothesis: *KCNMA1* and *CACNA1D* mRNAs are found in close proximity to be translated in the same neighborhood. **B.** Images of fluorescent puncta from RNA scope experiments showing *KCNMA1* mRNA in magenta, *CACNA1D* mRNA in cyan, and *GAPDH* mRNA in green. Right, magnification of three ROI. **C.** Comparison of mRNA density of *KCNMA1*, *CACNA1D*, and *GAPDH*. **D.** Correlation plot of mRNA abundance of *KCNMA1* and *CACNA1D* per cell. **E.** Correlation plot of mRNA abundance of *KCNMA1* and *GAPDH* per cell. **F.** Comparison of colocalization between *KCNMA1* mRNA and mRNA from *CACNA1D*, *GAPDH*, and scrambled images of *CACNA1D*. Data points are from n = 67 cells. Scale bar is 10 µm and 1 µm in the magnifications. Data were analyzed using ordinary one-way ANOVA with Dunnett's multiple comparisons test.

240

241 Probes against *GAPDH* mRNA were used as a control in the same cells that we probed
242 for *KCNMA1* and *CACNA1D* using the multiplex capability of this design. Transcripts were
243 detected at different expression levels. *GAPDH* and *CACNA1D* mRNAs were more abundant
244 (134 and 33 mRNA/100 µm^2, respectively) than *KCNMA1* mRNA (12 mRNA/100 µm^2, Figure 5C).
245 Interestingly, the abundance of *KCNMA1* transcripts correlated more with the abundance of
246 *CACNA1D* transcripts than with the abundance of *GAPDH*, though with a modest R^2 value (Figure

247 5D and E). Furthermore, *KCNMA1* and *CACNA1D* mRNA colocalized by 60 ± 4%, which was
248 20% more than with *GAPDH* mRNA (Figure 5F). As an additional control and to rule out the
249 potential influence of difference between *CACNA1D* and *KCNMA*1 abundance, we assessed
250 *CACNA1D* colocalization against randomized, computer-generated *KCNMA1* mRNA signals,
251 where localization was randomized while maintaining the same overall transcript count. The
252 significantly lower (20%) colocalization observed in scrambled conditions compared to genuine
253 BK-Cav1.3 mRNA interactions confirms that proximity is not an artifact of expression levels but
254 reflects a specific spatial association. These results suggest that some fraction of mRNAs for BK
255 and Ca_V1.3 channels are translated nearby, so the channel proteins potentially could be inserted
256 into the same regions of the ER. We suggest that the newly synthesized proteins remain together
257 during trafficking through the ER and the Golgi.
258
259 Next, we compared the proximity between *KCNMA1* and *SCN9A*. We detected *SCN9A* in
260 the same cells where *KCNMA1* was found (Figure 6A). The colocalization between *KCNMA1* and
261 *SCN9A* was only 18 ± 2% (Figure 6C), which was less than what was observed with *KCNMA1*
262 and *CACNA1D* (60%, Figure 5F). notably, we observed comparable levels of co-localization
263 between *KCNMA1* and *SCN9A* transcripts in both directions (data not shown), with no statistically
264 significant difference. These findings support the specificity of mRNA co-localization and that
265 *KCNMA1* tends to localize closer to *CACNA1D* than to *SCN9A* or *GAPDH*, supporting the
266 specificity of *KCNMA1* and *CACNA1D* mRNA association.
267 With the goal of understanding if this concept could apply to other channels, we used the
268 same approach to test a second protein known to provide calcium for BK channel opening. Similar
269 to the coupling between BK and Ca_V1.3 channels, RyR2 also can be structurally coupled to BK
270 channels [37]. Figure 6B shows high resolution images of single molecule in situ hybridization for
271 *RyR2* probed together with *KCNMA1* in INS-1 cells. In the same population of cells, *KCNMA1*
272 and *RyR2* colocalization was 27 ± 3%, which is 1.5 times that with *SCN9A* mRNA. We also
273 assessed *RyR2* colocalization with randomized, computer-generated *KCNMA1* mRNA signals.
274 We found that colocalization between randomized *KCNMA1* and genuine *RyR2* was 87% less
275 colocalized compared to the analysis of genuine *KCNMA1* and genuine *RyR2* (Figure 6C),
276 suggesting that *KCNMA1* not only colocalizes with *CACNA1D* but also with mRNA of other known
277 calcium sources.

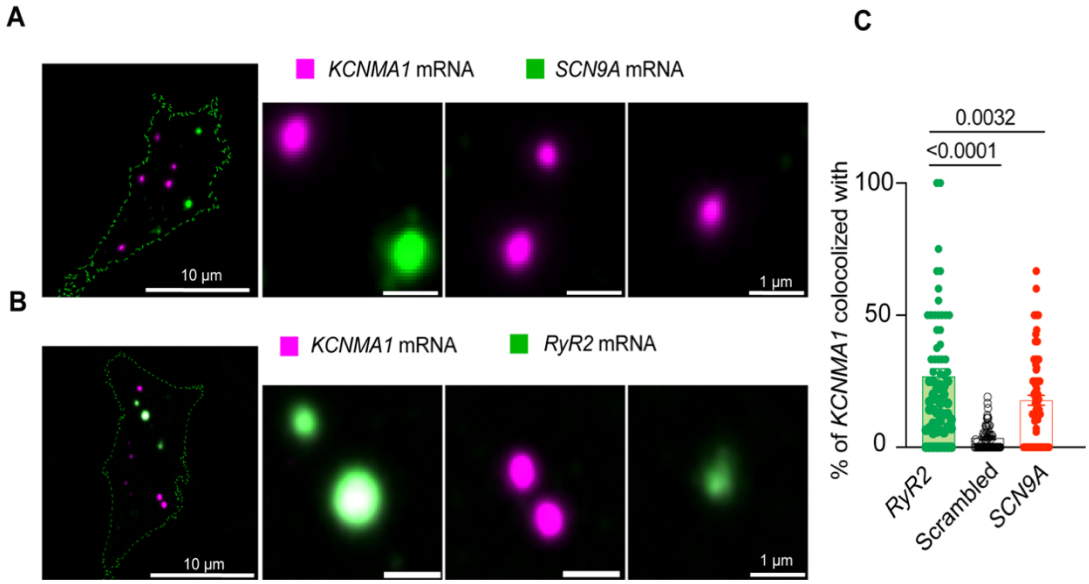

Figure 6. BK mRNA (*KCNMA1*) and RyR-2 mRNA (*RyR2*) colocalize. A. Representative confocal images of *KCNMA1* and $Na_V1.7$ (*SCN9A*) mRNA. **B.** Representative images of *KCNMA1* and *RyR2* mRNA. **C**. Comparison of the colocalization between *KCNMA1* mRNA and mRNA from *RyR2*, *SCN9A*, and scrambled images of *KCNMA1*. Data points are from n =67 cells. One way ANOVA. Scale bar is 10 µm and 1 µm in the magnifications. Data were analyzed using ordinary one-way ANOVA with Dunnett's multiple comparisons test.

To further investigate whether *KCNMA1* and *CACNA1D* are localized in regions of active translation (Figure 7A), we performed RNAscope targeting *KCNMA1* and *CACNA1D* alongside immunostaining for BK protein. This strategy enabled us to visualize transcript-protein colocalization in INS-1 cells with subcellular resolution.

By directly evaluating sites of active BK translation, we aimed to determine whether newly synthesized BK protein colocalized with *CACNA1D* mRNA signals (Figure 7A). Confocal imaging revealed distinct micro-translational complex where *KCNMA1* mRNA puncta overlapped with BK protein signals and were located adjacent to *CACNA1D* mRNA (Figure 7B). Quantitative analysis showed that 71 ± 3% of all *KCNMA1* colocalized with BK protein signal which means that they are in active translation. Interestingly, 69 ± 3% of the *KCNMA1* in active translation colocalized with *CACNA1D* (Figure 7C), supporting the existence of functional micro-translational complexes between BK and $Ca_V1.3$ channels.

291

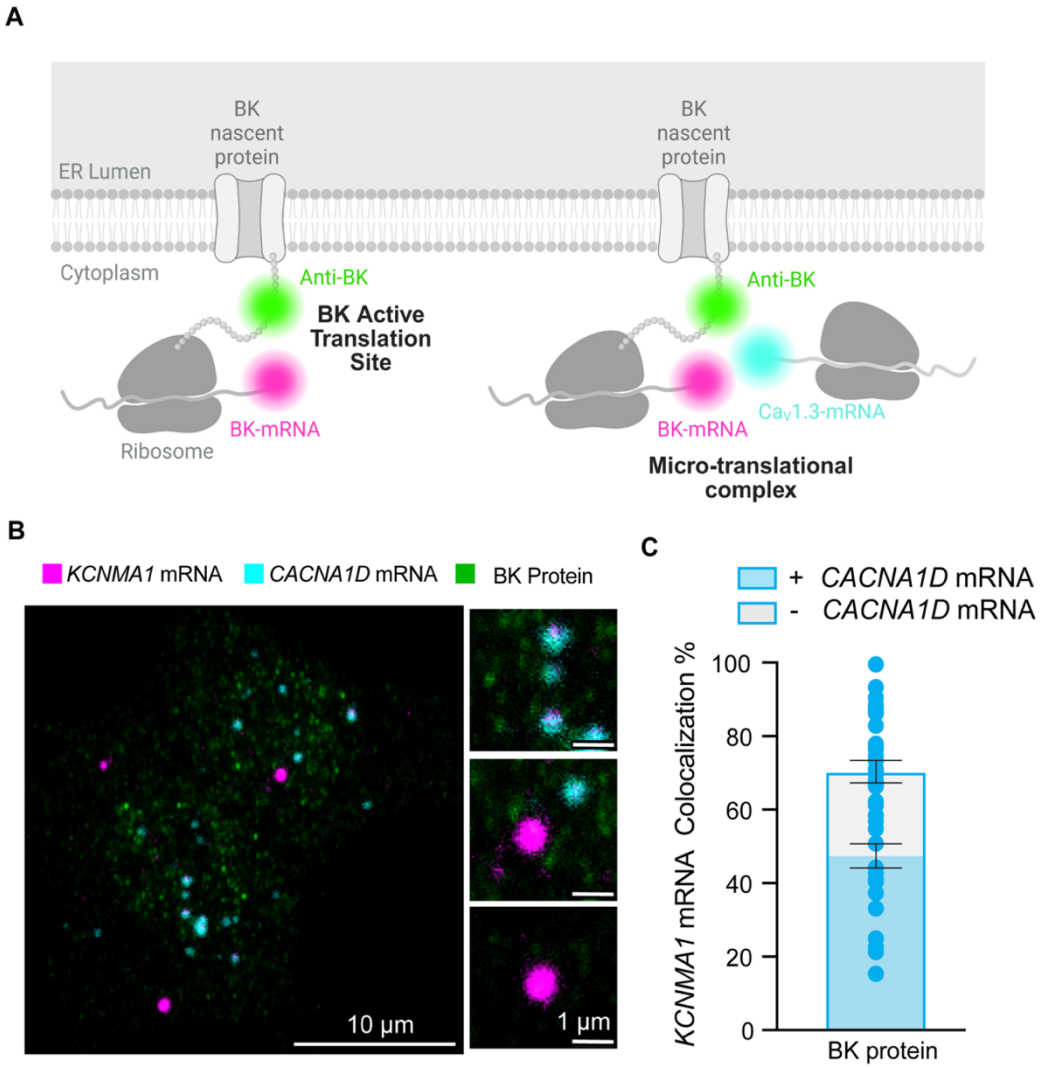

Figure 7. BK mRNA (*KCNMA1*) and $Ca_V1.3$ mRNA (*CACNA1D)* colocalize in micro-translational complexes. **A**. Diagram of the hypothesis: *KCNMA1* mRNAs are found in micro-translational complexes. **B.** Representative images of *KCNMA1* mRNA in magenta, *CACNA1D* mRNA in cyan, and BK protein in green. **C**. Comparison of the frequency of colocalization *KCNMA1* mRNA in active translation and in micro-translational complexes. Data points are from n = 57 cells. One way ANOVA was used as statistical analysis. Scale bar is 10 µm and 1 µm in the magnifications.

292

293 **BK and $Ca_V1.3$ channels form hetero-clusters at the plasma membrane of INS-1 cells.**

294 We previously showed the organization of BK and $Ca_V1.3$ channels in hetero-clusters in
295 tsA-201 cells and neurons, including hippocampal and sympathetic motor neurons [15]. Our
296 present study utilizes INS-1 cells. We detected single microscopy and determined their degree of
297 colocalization. Figure 8A shows a representative image of the localizations of antibodies against
298 BK and $Ca_V1.3$ channels. Maps were rendered at 5 nm, the pixel size for the images presented.
299 BK-positive pixels formed multi-pixel aggregates, which has been interpreted as homo-clusters of
300 molecules in INS-1 cells. It is important to note that this technique does not allow us to distinguish

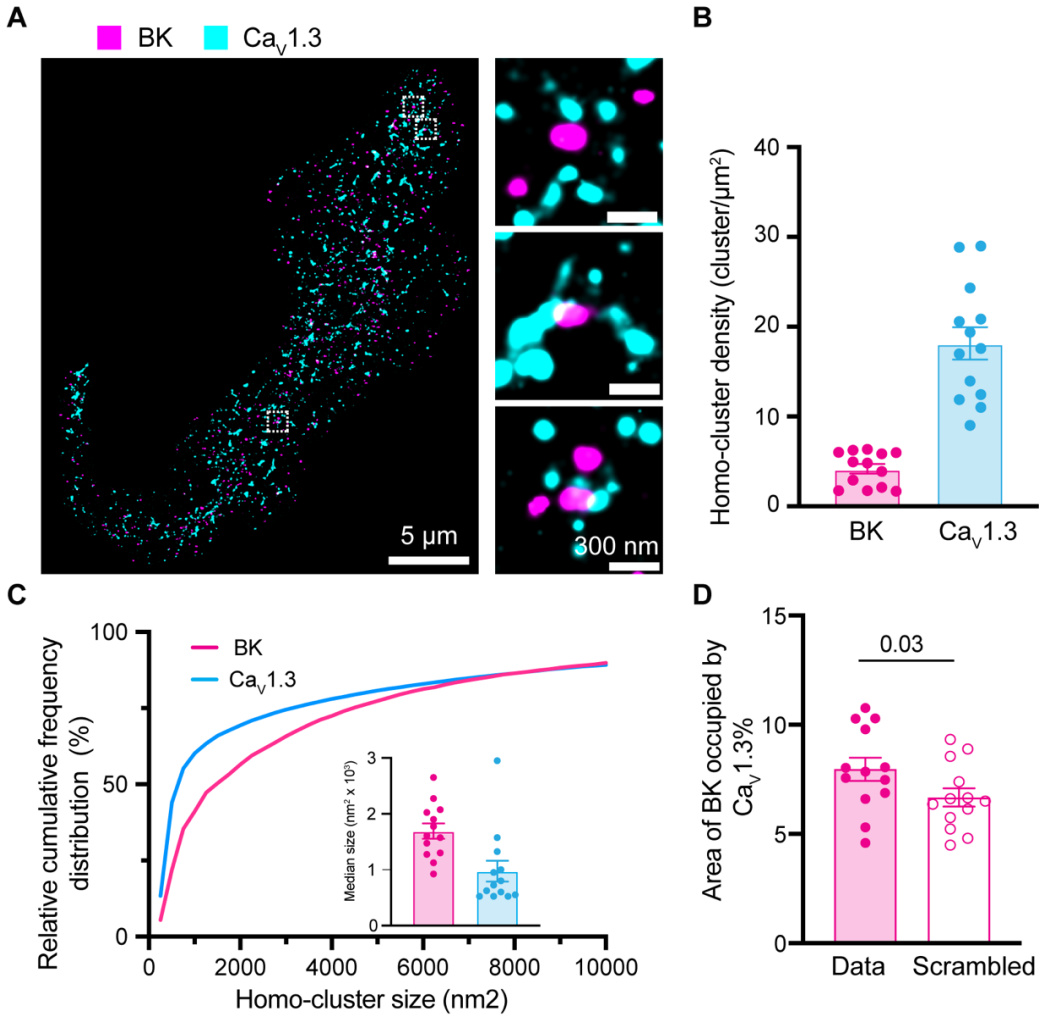

Figure 8. Formation of BK and Ca$_V$1.3 hetero-clusters in INS-1 cells. A. Representative localization map of antibodies against BK (magenta) and Ca$_V$1.3 (cyan) channels. Magnifications are shown in the insets on the right. **B.** Scatter dot plot of homo-cluster densities of BK and Ca$_V$1.3 channels in INS-1 cells. **C.** Cumulative frequency distributions of homo-cluster sizes of BK and Ca$_V$1.3 channels. Inset compares median size of BK and Ca$_V$1.3 homo-clusters. **D.** Comparison of colocalization between BK and Ca$_V$1.3 and between scrambled BK and Ca$_V$1.3. Data points are from n = 13 cells. Scale bar is 5 µm and 300 nm in the magnifications. Data was analyzed using paired t-tests to evaluate significance.

between labeling of four BK α-subunits within a tetramer and labeling of multiple BK channels in a cluster. Hence, particles smaller than ~1680 nm² may represent either a single tetramer or a cluster. This limitation applies to Figures 8C and 9D and does not affect measurements of BK–Ca$_V$1.3 proximity. Ca$_V$1.3 channels also formed homo-clusters. When looking at the formation of BK and Ca$_V$1.3 hetero-clusters, no fixed geometry or stoichiometry was observed. On the contrary, maps showed a distribution of distances between BK and Ca$_V$1.3 detected pixels. In some cases, BK and Ca$_V$1.3 channels were perfectly overlapping, as if the detection of the antibodies could not be separated by the 20 nm resolution. In other cases, BK

310 and $Ca_V1.3$ channels were adjacent (less than 5 nm), and in other cases, BK homo-clusters were
311 surrounded by a variable number of $Ca_V1.3$ channels.
312 To provide a more quantitative description of the maps, we measured cluster density,
313 cluster size, and colocalization. We used the particle analysis tool of the software ImageJ for
314 these measurements. In this analysis, a particle for represents positive pixels irrespective of the
315 number of pixels composed. INS-1 cells showed 4 times as many $Ca_V1.3$ particles as BK particles
316 (Figure 8B). Figure 8C shows the frequency distribution of particle size, where the median area
317 is 1691 nm^2 for BK and 975 nm^2 for $Ca_V1.3$. The colocalization between BK and $Ca_V1.3$ clusters
318 (Figure 8D) was 7.5%, a value higher than that obtained from scrambled image controls. Notably,
319 37 ± 3% BK channels are at 200 nm or less from one or more $Ca_V1.3$, while 15 ± 2% of $Ca_V1.3$
320 channels are at 200 nm or less from one or more BK (Figure 8-supplementary 1 Panel A).
321 Furthermore, the distribution of the nearest distance between BK and $Ca_V1.3$ in INS-1 cells
322 (Figure 8-supplementary 1 Panel B, magenta) shows a large proportion of BK channels (around
323 40%) at <50 nm from any $Ca_V1.3$ channels. Together, these results suggest that INS-1 cells also
324 exhibit nanodomains containing BK-$Ca_V1.3$ hetero-clusters at the plasma membrane.
325
326 **Hetero-clusters of BK and $Ca_V1.3$ channels are detected at the plasma membrane soon**
327 **after their expression.**
328 In light of our results, our current model is that BK and $Ca_V1.3$ hetero-clusters form prior
329 to their insertion into the plasma membrane. One prediction based on this model is that channels
330 inserted in the plasma membrane would appear as hetero-clusters already at early time points
331 after the start of their synthesis. To test this prediction, we transfected tsA-201 cells with BK and
332 $Ca_V1.3$ channels and performed a chase experiment to detect their presence at the plasma
333 membrane using super-resolution microscopy. We measured particle size, density, and
334 colocalization at 18, 24, and 48 hours after transfection. Notably, although the channels were
335 transfected simultaneously, BK particles were detected in the plasma membrane 18 hours after
336 transfection, whereas $Ca_V1.3$ particles were detected 24 hours after transfection (Figure 9A-C).
337 The distribution of BK and $Ca_V1.3$ particle size did not change with the time after transfection
338 (Figure 9D and E), in agreement with Sato et al., 2019 [30].
339 In support of our prediction, we found particles of $Ca_V1.3$ near BK particles as soon as the
340 expression of $Ca_V1.3$ channels was detected in the plasma membrane (24 hours after
341 transfection, enlarged Figure 9B). To test this hypothesis further, we compared plots of
342 localization preference at 24 and 48 hours. These plots were constructed by measuring the
343 percentage of $Ca_V1.3$ area occupying concentric regions of 20 nm width around BK particles.

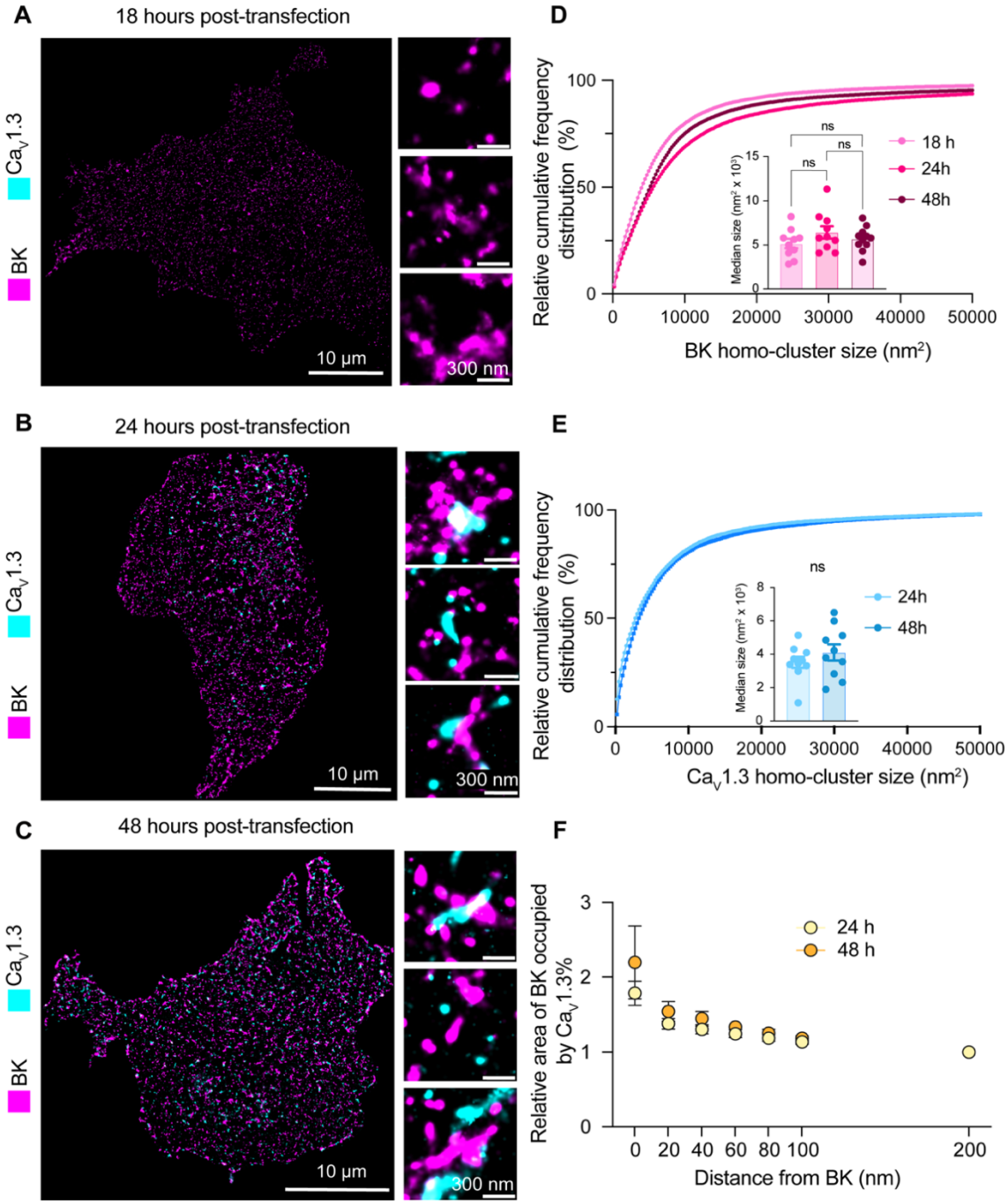

Figure 9. Hetero-clusters of BK and Ca$_V$1.3 channels are detected at the plasma membrane soon after their expression begins. A-C. Representative localization maps of antibodies against BK and Ca$_V$1.3 channels. (A) 18 hours, (B) 24 hours, or (C) 48 hours after DNA transfection into cells. Enlargements are shown in insets. **D.** Cumulative frequency distributions of BK homo-cluster size at 18, 24, and 48 hours. Inset compares median BK homo-cluster areas. **E.** Cumulative frequency distributions of Ca$_V$1.3 homo-clusters at 24 and 48 hours. Inset compares median Ca$_V$1.3 cluster areas. Ca$_V$1.3 clusters are not present at the 18-hour time point. **F.** Comparison of colocalization plots between BK and Ca$_V$1.3 channels at 24 and 48-hour time points. Data points are from n = 10 cells. Scale bar is 10 µm and 300 nm in enlargements. Statistical significance was assessed using ordinary one-way ANOVA followed by Dunnett's multiple comparisons test and unpaired t-test in panel D and E respectively.

Values were normalized to the percentage of colocalization found at 200 nm from BK. Figure 9F shows that the localization preference plots are identical at 24 and 48 hours, consistent with the hypothesis that both channels are inserted together into the plasma membrane already as hetero-clusters.

Discussion

Intracellular Assembly of BK and $Ca_V1.3$ Channels

Previous work from our group has revealed the organization of hetero-clusters of large-conductance calcium-activated potassium (BK) channels and voltage-gated calcium channels, particularly $Ca_V1.3$, within nanodomains [15]. This spatial organization is crucial for the functional coupling that enables BK channels to respond promptly to calcium influx, thereby modulating cellular excitability. While physical details of BK-$Ca_V1.3$ interactions are not fully elucidated, the evidence suggests that BK channels interact with both the Ca_V α1 subunit and its auxiliary subunits [38, 39].

Our findings highlight the intracellular assembly of BK-$Ca_V1.3$ hetero-clusters, though limitations in resolution and organelle-specific analysis prevent precise quantification of the proportion of intracellular complexes that ultimately persist on the cell surface. While our data confirms that hetero-clusters form before reaching the plasma membrane, it remains unclear whether all intracellular hetero-clusters transition intact to the membrane or undergo rearrangement or disassembly upon insertion. Future studies utilizing live cell tracking and high resolution imaging will be valuable in elucidating the fate and stability of these complexes after membrane insertion.

A stochastic model of ion channel homo-cluster formation in the plasma membrane proposes that random yet probabilistic interactions between ion channels contribute to their formation [30]. These clusters are stabilized and organized within specific membrane regions through biophysical mechanisms such as membrane curvature. Recent findings on spatial organization of G-protein coupled receptors provide additional support for this framework, demonstrating that the coupling of membrane proteins to the curvature of the plasma membrane acts as a driving force for their clustering into functional domains [40]. Yet, the mechanisms regulating the spatial organization of hetero-clusters are less known.

Colocalization and Trafficking Dynamics

The colocalization of BK and $Ca_V1.3$ channels in the ER and at ER exit sites before reaching the Golgi suggests a coordinated trafficking mechanism that facilitates the formation of

379 multi-channel complexes. This functional coupling is crucial for calcium signaling and membrane
380 excitability [41, 42]. Given the distinct roles of these compartments, colocalization at the ER and
381 ER exit sites may reflect transient proximity rather than stable interactions. Their presence in the
382 Golgi further suggests that post-translational modifications and additional assembly steps occur
383 before plasma membrane transport, providing further insight into hetero-cluster maturation and
384 sorting events. By examining BK-Ca_V1.3 hetero-cluster distribution across these trafficking
385 compartments, we ensure that observed colocalization patterns are considered within a broader
386 framework of intracellular transport mechanisms [43]. Previous studies indicate that ER exit sites
387 exhibit variability in cargo retention and sorting efficiency [44], emphasizing the need for careful
388 evaluation of colocalization data. Accounting for these complexities allows for a robust
389 assessment of signaling complexes formation and trafficking pathways.
390
391 **BK Surface Expression and Independent Trafficking Pathways**
392 BK surface expression in the absence of Ca_V1.3 indicates that its trafficking does not
393 strictly rely on Ca_V1.3-mediated interactions. Since BK channels can be activated by multiple
394 calcium sources, their presence in intracellular compartments suggests that their surface
395 expression is governed by intrinsic trafficking mechanisms rather than direct calcium-dependent
396 regulation. While some BK and Ca_V1.3 hetero-clusters assemble into signaling complexes
397 intracellularly, other BK channels follow independent trafficking pathways, demonstrating that
398 complex formation is not obligatory for all BK channels. Differences in their transport kinetics
399 further reinforce the idea that their intracellular trafficking is regulated through distinct
400 mechanisms. Studies have shown that BK channels can traffic independently of Ca_V1.3, relying
401 on alternative calcium sources for activation [13, 45]. Additionally, Ca_V1.3 exhibits slower
402 synthesis and trafficking kinetics than BK, emphasizing that their intracellular transport may not
403 always be coordinated. These findings suggest that BK and Ca_V1.3 exhibit both independent and
404 coordinated trafficking behaviors, influencing their spatial organization and functional interactions.
405 Future experiments using inducible constructs to precisely control transcription timing will enable
406 more precise quantification of hetero-cluster formation in the ER compartment prior to plasma
407 membrane insertion and reduce the variability introduced by differences in expression timing after
408 plasmid transfection.
409
410 **mRNA Colocalization and Protein Trafficking**
411 The colocalization of mRNAs encoding BK and Ca_V1.3 channels suggests a coordinated
412 translation mechanism that facilitates their proximal synthesis and subsequent assembly into

413 functional complexes. As a mechanism, mRNA localization enhances protein enrichment at
414 functional sites, coordinating with translational control to position ion channels at specific
415 subcellular domains; ion channel positioning is especially critical for neurons and cardiomyocytes
416 [46, 47]. By synthesizing these channels in close proximity, channels can be efficiently assembled
417 into functional units, making this process crucial for precise targeting and trafficking of ion
418 channels to specific subcellular domains, thereby ensuring proper cellular function and efficient
419 signal transduction [48-50]. Disruption in mRNA localization or protein trafficking can lead to ion
420 channel mislocalization, resulting in altered cellular function and disease [51, 52]. In cardiac cells,
421 precise trafficking of ion channels to specific membrane subdomains is crucial for maintaining
422 normal electrical and mechanical functions, and its disruption contributes to heart disease and
423 arrhythmias [53-55] Similarly, in neurons, the localization and translation of mRNA at synaptic
424 sites are essential for synaptic plasticity, and disturbances can lead to neurological disorders [56,
425 57].
426
427 **Co-translational Regulation and Functional Coordination**
428 The potential co-translational association of transcripts encoding BK and $Ca_V1.3$ ion
429 channels, as well as other known calcium sources like RyR2, may serve as a mechanism to
430 ensure the precise stoichiometry and assembly of functional channel complexes. It is important
431 to note that while our data suggest mRNA coordination, additional experiments are required to
432 directly assess co-translation. In parallel, the spatial organization of BK channels with other
433 calcium sources such as RyR2—particularly in airway myocytes—has been shown to facilitate
434 efficient BK activation by localized Ca^{2+} sparks [38]. Co-translational association of transcripts
435 encoding $K_V1.3$ channels was the first example in which the interaction of nascent $K_V1.3$ N-termini
436 facilitates proper tertiary and quaternary structure required for oligomerization [58, 59]. Similarly,
437 co-translational heteromeric association of hERG1a and hERG1b subunits ensures that cardiac
438 IK_r currents exhibit the appropriate biophysical properties and magnitude necessary for normal
439 ventricular action potential shaping [25]. The precise mechanism by which BK transcripts are
440 associated with the transcripts of calcium sources like $Ca_V1.3$ and RyR2 channels remain to be
441 elucidated. While it is conceivable that complementary base pairing or tertiary structural
442 interactions play a role, RNA binding proteins (RBPs) are likely key mediators of these
443 associations.
444
445 **Conclusion and Future Directions**

446 This study provides novel insights into the organization of BK and $Ca_V1.3$ channels in
447 hetero-clusters, emphasizing their assembly within the ER, at ER exit sites, and within the Golgi.
448 Our findings suggest that BK and $Ca_V1.3$ channels begin assembling intracellularly before
449 reaching the plasma membrane, shaping their spatial organization, and potentially facilitating
450 functional coupling. While this suggests a coordinated process that may contribute to functional
451 coupling, further investigation is needed to determine the extent to which these hetero-clusters
452 persist upon membrane insertion. While our study advances the understanding of BK and $Ca_V1.3$
453 hetero-cluster assembly, several key questions remain unanswered. What molecular machinery
454 drives this colocalization at the mRNA and protein level? How do disruptions to complex assembly
455 contribute to channelopathies and related diseases? Additionally, a deeper investigation into the
456 role of RNA binding proteins in facilitating transcript association and localized translation is
457 warranted.
458

459 **Acknowledgments**

460 We thank Gail Robertson for her immense support and influence in designing and
461 conducting this project. We thank Alexey Merz for his support and feedback through this project.
462 We thank Bertil Hille for his contribution to editing the writing of this project. We thank Martina
463 Hunt, Maria Elena Danoviz, Paula Martinez-Feduchi, Wendy Piñon-Teal, and Raul Riquelme for
464 reading and providing feedback on the manuscript. We thank William Catterall and Ruth E.
465 Westenbroek for providing the antibody against $Ca_V1.3$. This study was supported by the National
466 Institutes of Health MIRA R35 GM142690 to O.V. C.M. was supported by HL162609 and the
467 Freeman Hrabowski HHMI Scholars program.
468

469 **Materials and Methods**

470 Key resource table

Reagent type (species) or resource	Designation	Source or reference	Identifiers	Additional information
Cell line (human)	tsA-201	Sigma	RRID:CVCL_2737	Authentication: STR profiling; Mycoplasma: negative (see Materials & Methods).
Cell line (rat)	INS-1	Sigma	RRID:CVCL_0352	Authentication: STR profiling/DNA barcoding; Mycoplasma: negative (see Materials & Methods).
Recombinant DNA reagent	CaV1.3	Addgene	RRID:Addgene_49333; Addgene:49333	Plasmid expressing CACNA1D (rat).

Recombinant DNA reagent	Slo1 (BK)	Addgene	RRID:Addgene_113566; Addgene:113566	Mouse BK channel alpha subunit expression vector.
Recombinant DNA reagent	KDEL-mox-GFP (ERmoxGFP)	Addgene	RRID:Addgene_68072; Addgene:68072	ER-localized moxGFP with KDEL retention sequence.
Recombinant DNA reagent	pmGFP-Sec16	Addgene	RRID:Addgene_15775; Addgene:15775	pmGFP-Sec16S mammalian expression plasmid.
Recombinant DNA reagent	Golgi-mEGFP	Addgene	RRID:Addgene_182877; Addgene:182877	Golgi-targeted mEGFP.
Recombinant DNA reagent	pPH-PLC-δ-GFP (PH-PLCD1-GFP)	Addgene	RRID:Addgene_51407; Addgene:51407	Biosensor for PI(4,5)P2.
Recombinant DNA reagent	CaVβ3	Diane Lipscombe, Brown University	other	Auxiliary subunit for CaV1.3; repository ID not available; contact depositor.
Recombinant DNA reagent	CaVα2δ1	Diane Lipscombe, Brown University	other	Auxiliary subunit for CaV1.3; repository ID not available; contact depositor.
Sequence-based reagent (rat)	RNAscope 3-plex Positive Control Probes	Advanced Cell Diagnostics	Cat. No. 320871	Species-specific housekeeping targets for RNAscope; 3-plex positive control.
Sequence-based reagent (rat)	RNAscope 3-plex Negative Control Probe (dapB)	Advanced Cell Diagnostics	Cat. No. 320871	Negative control probe targeting bacterial dapB.
Sequence-based reagent (rat)	RNAscope™ Probe - Rn-Ryr	Advanced Cell Diagnostics	Cat. No. 2560931	Custom target probe.
Sequence-based reagent (rat)	RNAscope™ Probe - Rn-Scn9a	Advanced Cell Diagnostics	Cat. No. 317851	Custom target probe.
Sequence-based reagent (rat)	RNAscope Probe - Rn-Kcnma1-C3	Advanced Cell Diagnostics	Cat. No. 1108261-C3	Channel C3 probe.
Sequence-based reagent (rat)	RNAscope Probe - Rn-Cacna1d-C2	Advanced Cell Diagnostics	Cat. No. 409361-C2	Channel C2 probe.
Sequence-based reagent (rat)	RNAscope Probe - Rn-Gapdh	Advanced Cell Diagnostics	Cat. No. 409821	Housekeeping gene control.
Antibody	Anti-CaV1.3 (Rabbit polyclonal)	Drs. William Catterall and Ruth Westenbroek		Rabbit polyclonal primary recognizing residues 809–825 (II–III loop), (1:100), (1µl)
Antibody	Anti-Slo1 (clone L6/60) (Mouse monocolonal)	Millipore Sigma	RRID:AB_10805948; Cat. No. MABN70	Mouse monoclonal, (1:100), (1µl)
Antibody	Anti-GFP (Goat polyconolal)	Abcam	RRID:AB_305643; Cat. No. ab6673	Rabbit polyclonal to full-length Aequorea victoria GFP, (1:100), (1µl)
Antibody	Anti-58K Golgi (Mouse monoclonal)	Abcam	RRID:AB_2107005; Cat. No. ab27043	Mouse monoclonal recognizing Golgi protein (1:100), (1µl)

Antibody	Donkey anti-mouse Alexa 647 (Donkey polyclonal)	Invitrogen (Molecular Probes)	RRID:AB_2536183; Cat. No. A-31573	Secondary antibody donkey polyclonal, (1:1000), (1µl)
Antibody	Donkey anti-rabbit Alexa 555 (Donkey polyclonal)	Invitrogen (Molecular Probes)	RRID:AB_2534017; Cat. No. A10042	Secondary antibody, donkey polyclonal, (1:1000), (1µl)
Antibody	Donkey anti-goat Alexa 488 (Donkey polyclonal)	Invitrogen (Molecular Probes)	RRID:AB_162542; Cat. No. A-31571	Secondary antibody, donkey polyclonal, (1:1000), (1µl)
Antibody	Duolink® In Situ PLA® probe anti-rabbit PLUS (Donkey polyclonal)	Sigma	RRID:AB_2810940	Proximity ligation assay probe, donkey polyclonal, (1:20), (2µl)
Antibody	Duolink® In Situ PLA® probe anti-mouse PLUS (Donkey polyclonal)	Sigma	RRID:AB_2810939	Proximity ligation assay probe, donkey polyclonal, (1:20), (2µl)
Commercial assay or kit	Duolink® In Situ Red Starter Kit	Sigma	Cat. No. DUO92008	PLA detection kit.
Chemical compound, drug	Lipofectamine 3000	Invitrogen	Cat. No. L3000001/008/015 (series)	Transfection reagent; see Thermo Fisher catalog for sizes.
Chemical compound, drug	ProLong™ Gold Antifade Mountant with DAPI	Invitrogen	Cat. No. P36931	Mounting medium with DAPI.
Commercial assay or kit	RNAscope™ Multiplex Fluorescent v2 Assay	Advanced Cell Diagnostics (Bio-Techne)	Cat. No. 323270 (with TSA Vivid dyes) / 323100 (reagent kit v2)	Manual multiplex fluorescent RNA ISH assay.
Software, algorithm	Prism	GraphPad	RRID:SCR_002798	Version 10
Software, algorithm	Excel	Microsoft		Microsoft 365 build
Software, algorithm	ImageJ	NIH	RRID:SCR_003070	ImageJ2/Fiji build
Software, algorithm	NImOS	ONI		Version: v1.18.3

471

472 **Cell culture:**

473 We used tsA-201 cells to co-express BK and $Ca_V1.3$ channels heterologously. Cells were
474 grown in DMEM (Gibco) supplemented with 10% fetal bovine serum and 0.2%
475 penicillin/streptomycin. We used rat insulinoma (INS-1) cells to study endogenous levels of
476 transcripts and proteins of channels. INS-1 cells were cultured in RPMI high glutamate medium
477 (Gibco) with 10% fetal bovine serum, 0.2% penicillin/streptomycin, 10 mM HEPES (Gibco), 1 mM
478 sodium pyruvate (Gibco), and 50 μM 2-mercaptoethanol. Both cell types were passaged twice a
479 week and incubated in 5% CO_2 at 37°C. Cell lines tsA-201 (human) and INS-1 (rat) were
480 purchased from Sigma. According to the manufacturer, these cell lines were authenticated and
481 tested for mycoplasma contamination prior to shipment. No additional authentication or
482 contamination testing was performed by the authors.
483
484 **Plasmids and transfection:**
485 Cells were transfected with 0.1– 0.4 μg DNA per plasmid and plated for 24 hours on poly-
486 D-Lysine coated coverslips. Lipofectamine 3000 (Invitrogen, RRID: L30000) was used for the
487 transfection. DNA clones of $Ca_V1.3$, BK channels, PH-PLCδ GFP, ER moxGFP, pmGFP-Sec16S
488 and Golgi-mGFP were obtained from Addgene (RRID:SCR_002037). The $Ca_V1.3$ α subunit
489 construct used in our study corresponds to the rat $Ca_V1.3e$ splice variant containing exons 8a, 11,
490 31b, and 42a, with a deletion of exon 32. The BK channel construct corresponds to the VYR splice
491 variant of the mouse BKα subunit (KCNMA1). Auxiliary subunits for $Ca_V1.3$ channels, $Ca_Vβ3$ and
492 $Ca_Vα2δ1$ (from Diane Lipscombe, Brown University, RI), were transfected as well. No BK channel
493 auxiliary subunits were transfected.
494
495 **Antibodies:**
496 $Ca_V1.3$ channels were immuno-detected with a rabbit primary antibody recognizing
497 residues 809 to 825 located at the intracellular II-III loop of the channel
498 (DNKVTIDDYQEEAEDKD), kindly provided by Drs. William Catterall and Ruth Westenbroek [32].
499 BK channels were detected using the anti-Slo1 mouse monoclonal antibody clone L6/60. The
500 goat polyclonal GFP antibody was against the recombinant full-length protein corresponding to
501 *Aequorea victoria* GFP. Anti-58K Golgi protein antibody was used to mark the Golgi. Specificity
502 of antibodies was tested in un-transfected tsA-201 cells (Figure 2- Supplementary 1). The
503 secondary antibodies tagged with Alexa dyes were Donkey anti-mouse Alexa-647, Donkey anti-
504 rabbit Alexa-555, Donkey anti-goat Alexa-488 (Molecular Probes).

505

506 **Immunostaining:**

507 Cells were fixed with freshly prepared 4% paraformaldehyde for 10 minutes. After
508 washing, aldehydes were reduced with 0.1% $NaBH_4$ for 5 minutes and then washed again.
509 Nonspecific binding was blocked with 3% bovine serum albumin (Thermo Scientific). Cells were
510 permeabilized with 0.25% v/v Triton X-100 in PBS for 1 hour. Primary antibodies were used at 10
511 µg/ml in blocking solution and incubated overnight at 4°C. After washing, secondary antibodies
512 at 2 µg/ml were incubated for 1 hour at 21˚C. Washing steps indicated in all methods include 3
513 cycles of rinsing and rocking for 5 minutes with PBS at 21˚C. Cells were imaged using an inverted
514 AiryScan microscope or an ONI Nanoimager with super-resolution capabilities, in total internal
515 reflection fluorescence (TIRF) mode, and with a Z-resolution of 50 nm.

516

517 **Proximity ligation assay (PLA):**

518 Cells were fixed with freshly prepared 4% paraformaldehyde for 10 minutes. After
519 washing, aldehydes were reduced with 50 mM glycine for 15 minutes. After another round of
520 washes, PLA was performed according to manufacturer instructions (Duolink® In Situ Red Starter
521 Kit). Cells were blocked and permeabilized with Duolink blocking solution. Primary antibodies
522 were used at 10 µg/ml in Duolink antibody diluent and incubated overnight at 4°C. The Duolink®
523 In Situ PLA® probe anti-rabbit PLUS and anti-mouse MINUS were used as secondary antibodies,
524 followed by ligation and amplification. For PLA combined with immunostaining, PLA was followed
525 by a secondary antibody incubation with Alexa Fluor-488 at 2 µg/ml for 1 hour at 21˚C. Since GFP
526 fluorescence fades significantly during the PLA protocol, resulting in reduced signal intensity and
527 poor image resolution, GFP was labeled using an antibody rather than relying on its intrinsic
528 fluorescence. Coverslips were mounted using ProLong™ Gold Antifade Mountant with DAPI.
529 Cells were imaged using an inverted Zeiss AiryScan microscope.

530

531 **Single-molecule fluorescence in situ hybridization (RNAscope™):**

532 Manual RNAscope assay was performed using RNAscope Multiplex Fluorescent V2
533 Assay according to the manufacturer's protocol. The RNAscope assay consists of target probes
534 and a signal amplification system composed of a preamplifier, amplifier, and label probe. A
535 schematic RNAscope assay procedure is shown in Figure 5- Supplementary 1. The probes
536 against the mRNAs of interest and tested in this work were designed by Advanced Cell
537 Diagnostics. Briefly, cells were fixed with 4% paraformaldehyde for 30 minutes, washed,
538 dehydrated, and then rehydrated with ethanol, and permeabilized with 0.1% Tween-20 in PBS.

539 Next, cells were quenched with H_2O_2 and treated with Protease III. Probes were hybridized for 2
540 hours at 40°C followed by RNAscope amplification and then fluorescence detection. Coverslips
541 were mounted using ProLong™ Gold Antifade Mountant with DAPI. We used the following
542 RNAscope probes: RNAscope 3-plex Positive Control Probes, RNAscope 3-plex negative control
543 probes, RNAscope™ Probe- Rn-Ryr, RNAscope™ Probe- Rn-Scn9a, RNAscope Probe- Rn-
544 Kcnma1-C3, RNAscope Probe- Rn-Cacna1d-C2, and RNAscope Probe- Rn-Gapdh. Cells were
545 imaged on the inverted AiryScan microscope. For PLA and RNAscope experiments, we used
546 custom-made macros written in ImageJ. Processing of PLA data included background
547 subtraction. To assess colocalization, fluorescent signals were converted into binary images, and
548 channels were multiplied to identify spatial overlap. Specificity of RNAscope probes was tested in
549 un-transfected tsA-201 cells (Figure 5- Supplementary 2). For RNAscope combined with
550 immunostaining, RNAscope was followed by blocking in PBS supplemented with 0.01 % Tween-
551 20 and 3% BSA for 1 h at 21˚C. Samples were then probed for BK protein using primary antibody
552 overnight at 4˚C followed by secondary antibody incubation with Alexa Fluor-488 at 2 µg/ml for 1
553 hour at 21˚C. Coverslips were mounted using ProLong™ Gold Antifade Mountant. Cells were
554 imaged using an inverted Zeiss AiryScan microscope.
555
556 **High resolution imaging:**
557 Cells were imaged using an inverted AiryScan microscope (Zeiss LSM 880) run by ZEN
558 black v2.3 software and equipped with a plan apochromat 63X oil immersion objective with 1.4
559 NA. Fluorescent dyes were excited with a 405 nm diode, 458–514 nm argon, 561 nm, or 633 nm
560 laser. Emission light was detected using an Airyscan 32 GaAsP detector and appropriate
561 emission filter sets. The point spread functions were calculated using ZEN black software and 0.1
562 µm fluorescent microspheres. The temperature inside the microscope housing was 22°C. Images
563 were analyzed using ImageJ (NIH).
564
565 **Super-resolution imaging:**
566 Direct stochastic optical reconstruction microscopy (dSTORM) images of BK and $Ca_V1.3$
567 overexpressed in tsA-201 cells were acquired using an ONI Nanoimager microscope equipped
568 with a 100X oil immersion objective (1.4 NA), an XYZ closed-loop piezo 736 stage, and triple
569 emission channels split at 488, 555, and 640 nm. Samples were imaged at 35°C. For single-
570 molecule localization microscopy, fixed and stained cells were imaged in GLOX imaging buffer
571 containing 10 mM β-mercaptoethylamine (MEA), 0.56 mg/ml glucose oxidase, 34 µg/ml catalase,
572 and 10% w/v glucose in Tris-HCl buffer. Single-molecule localizations were filtered using NImOS

573 software (v.1.18.3, ONI). Localization maps were exported as TIFF images with a pixel size of 5
574 nm. Maps were further processed in ImageJ (NIH) by thresholding and binarization to isolate
575 labeled structures. To assess colocalization between the signal from two proteins, binary images
576 were multiplied. Particles smaller than 400 nm^2 were excluded from the analysis to reflect the
577 spatial resolution limit of STORM imaging (20 nm) and the average size of BK channels. To
578 examine spatial localization preference, binary images of BK were progressively dilated to 20 nm,
579 40 nm, 60 nm, 80 nm, 100 nm, and 200 nm to expand their spatial representation. These modified
580 images were then multiplied with the $Ca_V1.3$ channel to quantify colocalization and determine BK
581 occupancy at increasing distances from $Ca_V1.3$. To ensure consistent comparisons across
582 distance thresholds, data were normalized using the 200 nm measurement as the highest
583 reference value, set to 1.
584
585 **Image scrambling:**
586 Images were binarized as TIFF images, and their respective cell perimeter coordinates
587 were exported as CSV files by ImageJ. Processed binary images were then analyzed by our
588 SpotScrambler (https://github.com/jehuang2/SpotScramble) Python program. SpotScrambler first
589 extracts the areas of fluorescent particles in the binary image. SpotScrambler then redraws the
590 fluorescent particles as circles at randomized coordinates within cell perimeter boundaries.
591 SpotScrambler accurately preserves particle number and particle sizes, averaging less than 1%
592 difference in total area of fluorescent particles between pre-SpotScrambler and post-
593 SpotScrambler images. To ensure reliable randomization for each experiment, results were
594 averaged between 3 trials of SpotScrambler.
595
596 **Data analysis**
597 Excel (Microsoft), and Prism (GraphPad) were used to analyze data. ImageJ was used to
598 process images. One-way ANOVA and non-parametric statistical test (Mann-Whitney Wilcoxon)
599 were used to test for statistical significance. p-values <0.05 were deemed statistically significant.
600 The number of cells used for each experiment is detailed in each figure legend.

601 **Materials Availability Statement**

602 All newly created materials used in this study are available for public access. Plasmid constructs
603 have been deposited in Addgene (repository links and RRIDs are provided in the Methods
604 section). RNA probes utilized for in situ hybridization are proprietary to ACD Biotechnology and
605 are not accessible for redistribution. Complete details regarding materials, including catalog

606 numbers and RRIDs, are provided in the Methods section and in the Supporting Data Excel
607 sheet.

608 All datasets supporting the findings of this study have been deposited in Dryad and are publicly
609 available in dryad (https://doi.org/10.5061/dryad.63xsj3vfq)

610

611

612 **Supplementary Figure**

613

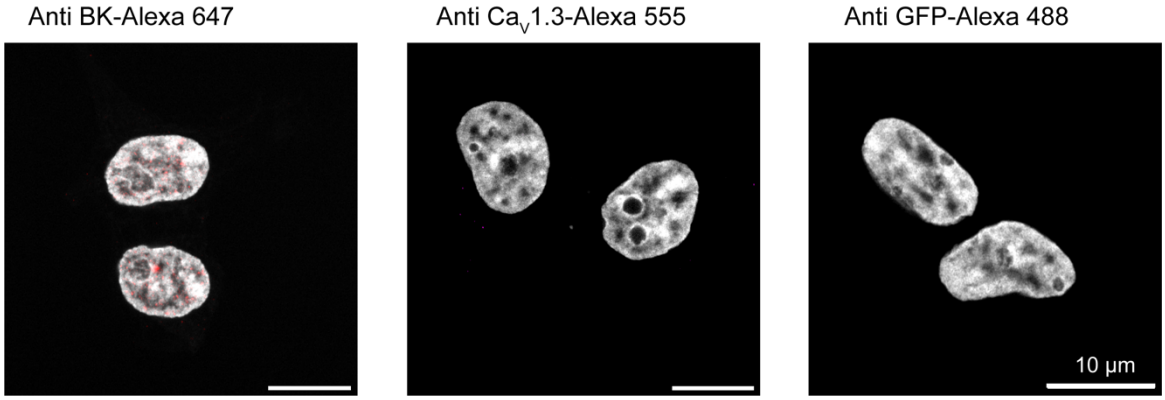

614

615 **Figure 2-Supplementary 1. Validation of antibodies against BK, Ca_V1.3 and GFP.** Representative confocal images
616 of tsA-201 cells immuno-tested for BK channels (left), Ca_V1.3 channels (middle), and GFP proteins (right). Cells were
617 not transfected. Nuclei were stained with DAPI and pseudo colored in gray. Scale bar is 10 µm for all images.

618

619

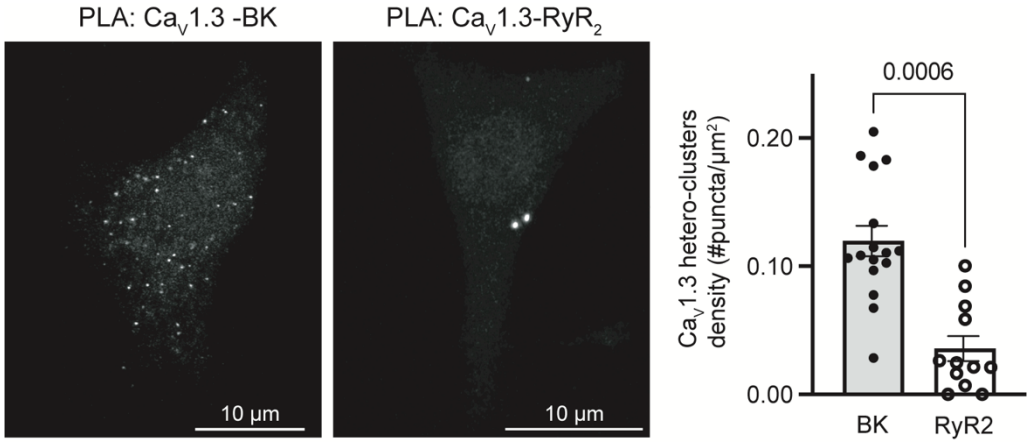

620

621 **Figure 4-Supplementary 1. Ca_V1.3 channels do not exhibit proximity interactions with ryanodine receptor type**
622 **2 (RyR_2). A.** Representative images of proximity ligation assay (PLA) experiments in INS-1 cells labeling against Ca_V1.3
623 and BK channels (left) or Ca_V1.3 and RyR_2 (right). Comparison of PLA puncta density for the two conditions. Statistical
624 significance was assessed using an unpaired t-test.

625

626

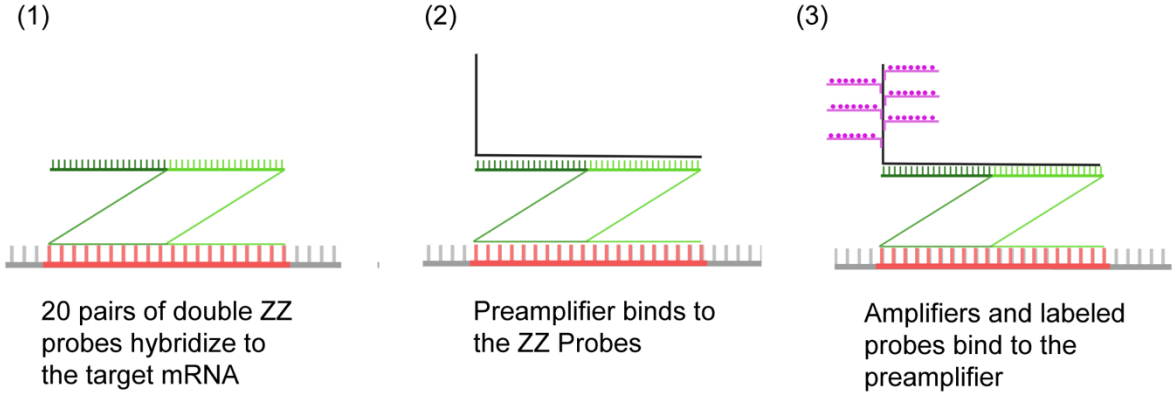

627 **Figure 5-Supplementary 1. Illustration of RNA scope methodology.** Steps to detect an mRNA sequence (red
628 zipper) consisting of (1) hybridization, (2) pre-amplification, (3) and labeling. Double ZZ probes are shown in green.
629 Dye labeling the mRNA is shown in magenta.

630

631

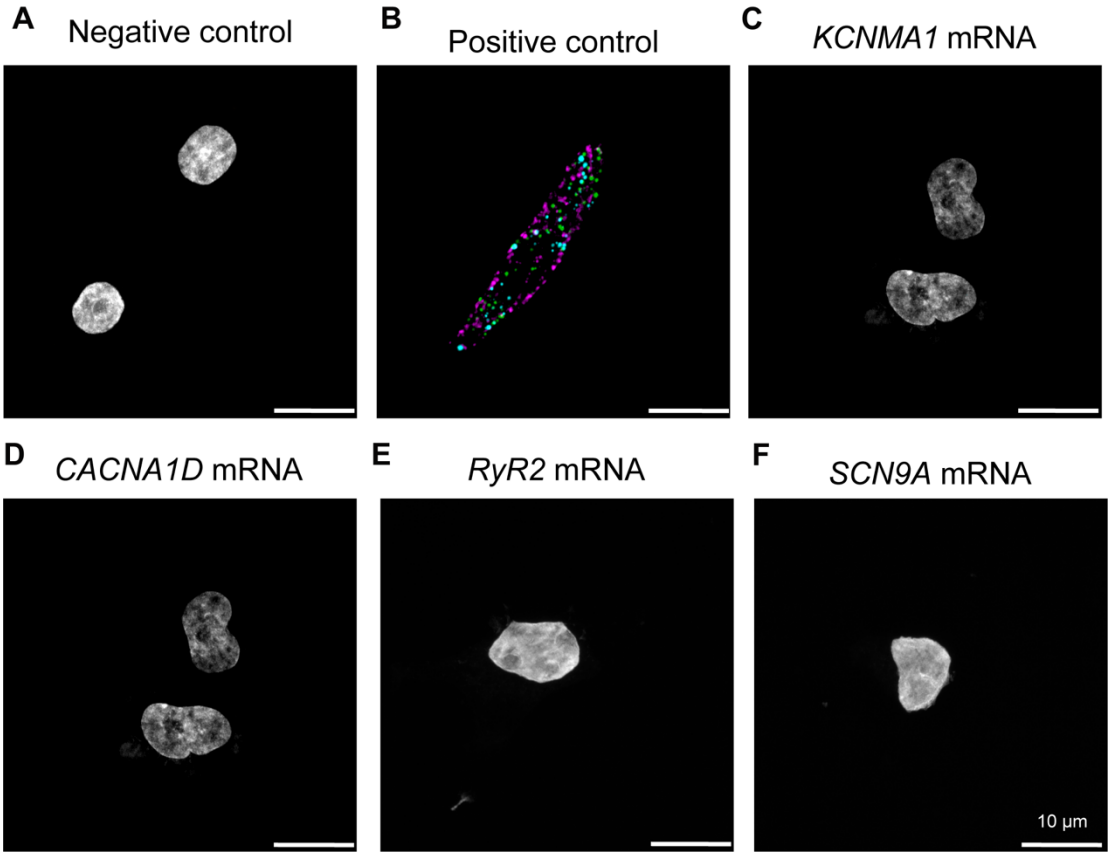

632

633 **Figure 5-Supplementary 2. RNA probe validation. A.** Representative images of INS-1 cells subjected to mRNA
634 probes against a bacterial gene (DapB from *Bacillus subtilis*). **B.** Representative images of INS-1 cells subjected to
635 mRNA probes against three constitutive mammalian genes (ubiquitin C, cyclophilin B, and a polymerase II subunit). **C**

636 **- F** show tsA-201 cells that were naive to exogenous DNA but treated with mRNA probes against the genes for (**C**)
637 BK channels, (**D**) $Ca_V1.3$ channels, (**E**) Ryanodine Receptors type 2 (RyR2), and (**F**) $Na_V1.7$ channels. Scale bar is
638 10 µm.
639

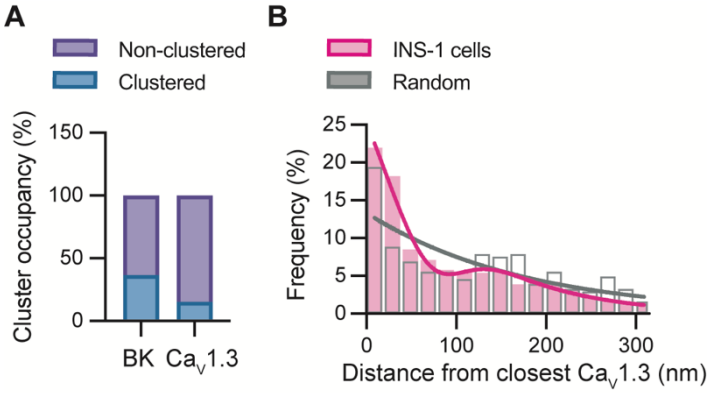

640
641 **Figure 8-Supplementary 1. Organization of BK-Ca_V1.3 hetero-clusters in INS-1 cells. A.** Proportion of channels in
642 clusters or outside clusters for BK and $Ca_V1.3$. Clustered channels were defined as being at a distance of 200 nm or
643 less from the other channel type. Channels found at 200 nm or more were considered non-clustered. Data from 7 cells.
644 **B.** Distribution of the nearest neighbor distance from BK channels to $Ca_V1.3$ channels in INS-1 cells (magenta, n =
645 1037 BK channels, from N = 5 cells). Distribution of the nearest neighbor distance from BK channels to randomized
646 channels (gray, n = 363 BK channels). The shift in the distribution from INS-1 cells to randomized images suggests a
647 preferential localization of endogenous BK-$Ca_V1.3$ hetero-clusters.
648

649

650 **References:**

651

652 1. Contreras, G.F., et al., *A BK (Slo1) channel journey from molecule to physiology.*
653 Channels (Austin), 2013. **7**(6): p. 442-58.
654 2. Kaczorowski, G.J., et al., *High-conductance calcium-activated potassium channels;*
655 *structure, pharmacology, and function.* J Bioenerg Biomembr, 1996. **28**(3): p. 255-67.
656 3. Contet, C., et al., *BK Channels in the Central Nervous System.* Int Rev Neurobiol,
657 2016. **128**: p. 281-342.
658 4. Ancatén-González, C., et al., *Ca^{2+} and Voltage-Activated K^{+} (BK) Channels in the*
659 *Nervous System: One Gene, a Myriad of Physiological Functions.* Int J Mol Sci, 2023.
660 **24**(4).
661 5. Dopico, A.M., A.N. Bukiya, and J.H. Jaggar, *Calcium- and voltage-gated BK channels*
662 *in vascular smooth muscle.* Pflugers Arch, 2018. **470**(9): p. 1271-1289.
663 6. Hu, S.L., H.S. Kim, and A.Y. Jeng, *Dual action of endothelin-1 on the Ca^{2+}-activated*
664 *K^{+} channel in smooth muscle cells of porcine coronary artery.* Eur J Pharmacol, 1991.
665 **194**(1): p. 31-6.
666 7. Semenov, I., et al., *BK channel beta1-subunit regulation of calcium handling and*
667 *constriction in tracheal smooth muscle.* Am J Physiol Lung Cell Mol Physiol, 2006.
668 **291**(4): p. L802-10.
669 8. Dupont, C., et al., *BK channels promote action potential repolarization in skeletal*
670 *muscle but contribute little to myotonia.* Pflugers Arch, 2024. **476**(11): p. 1693-1702.
671 9. Pallotta, B.S., K.L. Magleby, and J.N. Barrett, *Single channel recordings of Ca^{2+}-*
672 *activated K^{+} currents in rat muscle cell culture.* Nature, 1981. **293**(5832): p. 471-4.
673 10. Meredith, A.L., *BK Channelopathies andand KCNMA1-Linked Disease Models.* Annu
674 Rev Physiol, 2024. **86**: p. 277-300.
675 11. Bailey, C.S., et al., *KCNMA1-linked channelopathy.* J Gen Physiol, 2019. **151**(10): p.
676 1173-1189.
677 12. Houamed, K.M., I.R. Sweet, and L.S. Satin, *BK channels mediate a novel ionic*
678 *mechanism that regulates glucose-dependent electrical activity and insulin secretion*
679 *in mouse pancreatic beta-cells.* J Physiol, 2010. **588**(Pt 18): p. 3511-23.
680 13. Shah, K.R., X. Guan, and J. Yan, *Structural and Functional Coupling of Calcium-*
681 *Activated BK Channels and Calcium-Permeable Channels Within Nanodomain*
682 *Signaling Complexes.* Front Physiol, 2021. **12**: p. 796540.

683 14. Berkefeld, H., et al., *BKCa-Ca_V channel complexes mediate rapid and localized Ca^{2+}-*
684 *activated K^+ signaling.* Science, 2006. **314**(5799): p. 615-20.
685 15. Vivas, O., et al., *Proximal clustering between BK and Ca_V1.3 channels promotes*
686 *functional coupling and BK channel activation at low voltage.* Elife, 2017. **6**.
687 16. Prakriya, M. and C.J. Lingle, *Activation of BK channels in rat chromaffin cells requires*
688 *summation of Ca(2+) influx from multiple $Ca^{(2+)}$ channels.* J Neurophysiol, 2000. **84**(3):
689 p. 1123-35.
690 17. Lipscombe, D., T.D. Helton, and W. Xu, *L-type calcium channels: the low down.* J
691 Neurophysiol, 2004. **92**(5): p. 2633-41.
692 18. Chen, G., et al., *BK channel modulation by positively charged peptides and auxiliary*
693 *γ subunits mediated by the Ca^{2+} bowl site.* Journal of General Physiology, 2023.
694 **155**(6).
695 19. Brenner, R., et al., Cloning and functional characterization of novel large conductance
696 calcium-activated potassium channel beta subunits, hKCNMB3 and hKCNMB4. J Biol
697 Chem, 2000. 275(9): p. 6453-61.
698 20. Dudem, S., et al., Oxidation modulates LINGO2-induced inactivation of large
699 conductance, $Ca^{(2+)}$-activated potassium channels. J Biol Chem, 2023. 299(3): p.
700 102975.
701 21. Dudem, S., et al., LINGO1 is a regulatory subunit of large conductance, Ca^{2+} activated
702 potassium channels. Proceedings of the National Academy of Sciences, 2020. 117(4):
703 p. 2194-2200.
704 22. Knaus, H.G., et al., Primary sequence and immunological characterization of beta-
705 subunit of high conductance $Ca^{(2+)}$-activated K^+ channel from smooth muscle. J Biol
706 Chem, 1994. 269(25): p. 17274-8.
707 23. Yan, J. and R.W. Aldrich, LRRC26 auxiliary protein allows BK channel activation at
708 resting voltage without calcium. Nature, 2010. 466(7305): p. 513-6.
709 24. Yan, J. and R.W. Aldrich, BK potassium channel modulation by leucine-rich repeat-
710 containing proteins. Proceedings of the National Academy of Sciences, 2012. 109(20):
711 p. 7917-7922.
712 25. Liu, F., et al., *Cotranslational association of mRNA encoding subunits of heteromeric*
713 *ion channels.* Proc Natl Acad Sci U S A, 2016. **113**(17): p. 4859-64.
714 26. Eichel, C.A., et al., *A microtranslatome coordinately regulates sodium and potassium*
715 *currents in the human heart.* eLife, 2019. **8**: p. e52654.

716 27. Yang, S., et al., *Membrane curvature governs the distribution of Piezo1 in live cells.*
717 Nature Communications, 2022. **13**(1): p. 7467.
718 28. Chen, Z., et al., *EMC chaperone–Ca_V structure reveals an ion channel assembly*
719 *intermediate.* Nature, 2023. **619**(7969): p. 410-419.
720 29. Cheng, E.P., et al., *Restoration of Normal L-Type Ca^{2+} Channel Function During*
721 *Timothy Syndrome by Ablation of an Anchoring Protein.* Circulation Research, 2011.
722 **109**(3): p. 255-261.
723 30. Sato, D., et al., *A stochastic model of ion channel cluster formation in the plasma*
724 *membrane.* J Gen Physiol, 2019. **151**(9): p. 1116-1134.
725 31. Lu, J., et al., *T1-T1 interactions occur in ER membranes while nascent K_V peptides*
726 *are still attached to ribosomes.* Biochemistry, 2001. **40**(37): p. 10934-46.
727 32. Hell, J.W., et al., *Identification and differential subcellular localization of the neuronal*
728 *class C and class D L-type calcium channel alpha 1 subunits.* J Cell Biol, 1993. **123**(4):
729 p. 949-62.
730 33. Costantini, L.M., et al., *A palette of fluorescent proteins optimized for diverse cellular*
731 *environments.* Nat Commun, 2015. **6**: p. 7670.
732 34. Georgiades, P., et al., *The flexibility and dynamics of the tubules in the endoplasmic*
733 *reticulum.* Sci Rep, 2017. **7**(1): p. 16474.
734 35. Nixon-Abell, J., et al., *Increased spatiotemporal resolution reveals highly dynamic*
735 *dense tubular matrices in the peripheral ER.* Science, 2016. **354**(6311).
736 36. Bashour, A.M. and G.S. Bloom, *58K, a microtubule-binding Golgi protein, is a*
737 *formiminotransferase cyclodeaminase.* J Biol Chem, 1998. **273**(31): p. 19612-7.
738 37. Lifshitz, L.M., et al., *Spatial organization of RYRs and BK channels underlying the*
739 *activation of STOCs by $Ca^{(2+)}$ sparks in airway myocytes.* J Gen Physiol, 2011. **138**(2):
740 p. 195-209.
741 38. Rehak, R., et al., *Low voltage activation of KCa1.1 current by Ca_V3-KCa1.1*
742 *complexes.* PLoS One, 2013. **8**(4): p. e61844.
743 39. Zhang, F.X., et al., *BK Potassium Channels Suppress Cavα2δ Subunit Function to*
744 *Reduce Inflammatory and Neuropathic Pain.* Cell Rep, 2018. **22**(8): p. 1956-1964.
745 40. Kockelkoren, G., et al., *Molecular mechanism of GPCR spatial organization at the*
746 *plasma membrane.* Nat Chem Biol, 2024. **20**(2): p. 142-150.
747 41. Berkefeld, H., B. Fakler, and U. Schulte, Ca^{2+}-activated K^+ channels: from protein
748 complexes to function. Physiol Rev, 2010. 90(4): p. 1437-59.

749 42. Loane, D.J., P.A. Lima, and N.V. Marrion, Co-assembly of N-type Ca^{2+} and BK
750 channels underlies functional coupling in rat brain. J Cell Sci, 2007. 120(Pt 6): p. 985-
751 95.
752 43. Boncompain, G. and F. Perez, *The many routes of Golgi-dependent trafficking.*
753 Histochemistry and Cell Biology, 2013. **140**(3): p. 251-260.
754 44. Kurokawa, K. and A. Nakano, *The ER exit sites are specialized ER zones for the*
755 *transport of cargo proteins from the ER to the Golgi apparatus.* The Journal of
756 Biochemistry, 2019. **165**(2): p. 109-114.
757 45. Chen, A.L., et al., Calcium-Activated Big-Conductance (BK) Potassium Channels
758 Traffic through Nuclear Envelopes into Kinocilia in Ray Electrosensory Cells. Cells,
759 2023. 12(17): p. 2125.
760 46. Vacher, H., D.P. Mohapatra, and J.S. Trimmer, *Localization and targeting of voltage-*
761 *dependent ion channels in mammalian central neurons.* Physiol Rev, 2008. **88**(4): p.
762 1407-47.
763 47. Medioni, C., K. Mowry, and F. Besse, *Principles and roles of mRNA localization in*
764 *animal development.* Development, 2012. **139**(18): p. 3263-76.
765 48. Blandin, C.E., et al., *Remodeling of Ion Channel Trafficking and Cardiac Arrhythmias.*
766 Cells, 2021. **10**(9).
767 49. Dai, G., *Signaling by Ion Channels: Pathways, Dynamics and Channelopathies.* Mo
768 Med, 2023. **120**(5): p. 367-373.
769 50. Wang, J., et al., *RNA trafficking and subcellular localization—a review of mechanisms,*
770 *experimental and predictive methodologies.* Briefings in Bioinformatics, 2023. **24**(5):
771 p. bbad249.
772 51. Wang, E.T., et al., *Dysregulation of mRNA Localization and Translation in Genetic*
773 *Disease.* The Journal of Neuroscience, 2016. **36**(45): p. 11418.
774 52. Jameson, M.B., et al., *Pairwise biosynthesis of ion channels stabilizes excitability and*
775 *mitigates arrhythmias.* Proc Natl Acad Sci U S A, 2023. **120**(42): p. e2305295120.
776 53. Anderson, C.L., et al., *Most LQT2 mutations reduce K_V11.1 (hERG) current by a class*
777 *2 (trafficking-deficient) mechanism.* Circulation, 2006. **113**(3): p. 365-73.
778 54. Smyth, J.W. and R.M. Shaw, *Forward trafficking of ion channels: what the clinician*
779 *needs to know.* Heart Rhythm, 2010. **7**(8): p. 1135-40.
780 55. Basheer, W.A. and R.M. Shaw, *Connexin 43 and Ca_V1.2 Ion Channel Trafficking in*
781 *Healthy and Diseased Myocardium.* Circ Arrhythm Electrophysiol, 2016. **9**(6): p.
782 e001357.

783 56. Eliscovich, C., S.M. Shenoy, and R.H. Singer, *Imaging mRNA and protein interactions*
784 *within neurons.* Proc Natl Acad Sci U S A, 2017. **114**(10): p. E1875-E1884.
785 57. Yoon, Y.J., et al., *Glutamate-induced RNA localization and translation in neurons.* Proc
786 Natl Acad Sci U S A, 2016. **113**(44): p. E6877-E6886.
787 58. Robinson, J.M. and C. Deutsch, *Coupled tertiary folding and oligomerization of the T1*
788 *domain of K_V channels.* Neuron, 2005. **45**(2): p. 223-32.
789 59. Tu, L. and C. Deutsch, *Evidence for dimerization of dimers in K^+ channel assembly.*
790 Biophys J, 1999. **76**(4): p. 2004-17.